MAGNETIC BUBBLE CHAMBER PROTOTYPE DEVELOPMENT

A Dissertation

by

HAO CHEN

Submitted to the Office of Graduate and Professional Studies of
Texas A&M University
in partial fulfillment of the requirements for the degree of

DOCTOR OF PHILOSOPHY

Chair of Committee,	Rupak Mahapatra
Committee Members,	Michael Nippe
	Nader Mirabolfathi
	Louis Strigari
Head of Department,	Grigory Rogachev

December 2019

Major Subject: Physics

ABSTRACT

It is now evident that the majority of matter in our universe is composed of non-luminous dark matter. However, the nature of this dark matter remains mysterious. The most promising candidates for dark matter include axions and weakly interacting massive particles (WIMPs).

Current leading direct search experiments like SuperCDMS and LUX are located deep underground to shield against cosmic rays. They utilize extremely sensitive detectors to directly detect dark matter interacting with normal matter. Current experiments have quite poor sensitivity to detect low mass dark matter candidates due to the fact that the threshold of current detectors is not low enough. Low threshold detection techniques can also help study coherent neutrino-nucleus scattering.

As a result, new detection principles with a lower threshold are needed. Different materials such as silicon, germanium, xenon, etc. have been used as detectors and work well in the projects mentioned above, but searching for new detector materials could open the door to low threshold detection.

Single-molecule magnet (SMM) has long been known and researched. One of its most interesting phenomena is the magnetic avalanche. In this work, we tested the idea of using SMM materials to detect particles.

The experiment was operated in a cryogenic refrigerator at a temperature as low as 0.5 Kelvin, since magnetic avalanches can only happen at cryogenic temperatures. The main purpose is to prove the concept that magnetic avalanches can be triggered by the scattering of particles. Our data showed that high energy alpha particles were able to ignite magnetic avalanches in Mn12-acetate, one kind of SMM material.

With the long list of different kinds of SMMs, and the ability to synthesize new kinds according to our needs, it will be a promising way to detect dark matter, neutrinos, or other low energy particle interactions.

DEDICATION

To my family, Xinyi, Owen, Ian, my parents, and my grandparents.

ACKNOWLEDGMENTS

I would like to thank My advisor, Dr. Rupak Mahapatra, for guiding me through the learning and research process, advising and encouraging me whenever the experiments did not go in the right way.

I would like to thank my lab partner, Minjie Lu, who showed me many skills to work with a cryogenic refrigerator. He was always there whenever I needed an extra hand.

I would like to thank Dr. Glenn Agnolet who allowed me to use his refrigerator to conduct this experiment and gave me a lot of valuable advice.

I would like to thank Mark Platt, who helped me solve many equipment problems.

I would like to thank Andrew Jastram and Andy Kubik, who also provided a lot of valuable advice for my experiment and helped me to use various equipment required for the experiment.

I cannot finish my work without help from all the people mentioned here. I am grateful to work in our group.

Finally, I would like to thank Phil Bunting, Gabrielle Risica and Dr. Nippe for providing the necessary SMM crystals for this experiment.

CONTRIBUTORS AND FUNDING SOURCES

Contributors

This work was supervised by a dissertation committee consisting of Professor Rupak Mahapatra [advisor], Professor Nader Mirabolfathi, Professor Louis Strigari of the Department of Physics & Astronomy and Professor Michael Nippe of the Department of Chemistry

All other work conducted for the dissertation was completed by the student independently.

Funding Sources

This study is supported by the Texas A&M University College of Science for funding the entire work through the Strategic Transfomative Research Program (STRP).

NOMENCLATURE

SI	spin-independent
SD	spin-dependent
SMM	single-molecule magnet
OFHC	oxygen-free high thermal conductivity
MOND	modified Newtonian dynamics
MACHO	massive astrophysical compact halo object
WIMPs	weakly interacting massive particles
TES	transition edge sensors
iZIP	interleaved Z-sensitive Ionization Phonon
TPC	time projection chamber
PMT	photomultiplier tubes
GPIB	general Purpose Interface Bus
SQUID	superconducting quantum interference device
XRD	X-ray powder diffraction

TABLE OF CONTENTS

Page

LIST OF FIGURES

FIGURE Page

LIST OF TABLES

TABLE Page

1. INTRODUCTION

1.1 Dark Matter Introduction

Human beings have always been thinking about what our universe is made of. One reason is our inborn curiosity, and the other is more practical: the more we know about our surroundings, the better we can fit in and live. After the discovery of the Higgs boson, the standard model seems to stand solid to answer many of these questions, but there are several problems which still remain mysterious. The dark matter enigma is one of them.

1.1.1 Dark Matter Enigma

Early in the 20th century, astronomers used the mass-luminosity relation to determine the mass of remote stars. With apparent brightness and distance of a star from the earth, actual luminosity can be determined. Then One can calculate the mass of the star with the mass-luminosity relation. However, when people started to figure out the mass of galaxies or clusters with dynamic information, there was a huge discrepancy, which leads to the study of the dark matter.

The first modern evidence for dark matter was given by Dutch astronomer Jan Hendrik Oort in 1932. He studied the motion of stars in the Milky way, utilizing the Doppler effect. He postulated the majority of mass in the Milky way is dark matter [1].

The more famous evidence from Swiss astronomer F. Zwicky was brought up the very next year, 1933. When he examined the motion of about 1000 galaxies in the Coma galaxy cluster, He measured velocity information also from the Doppler shift. He ingeniously used the virial theorem to calculate the total mass of the cluster, assuming that the gravitational force is the only interaction between galaxies. When he compared his calculation with the result from the mass--luminosity relation, it showed the amount of non-luminous matter is much bigger than that of luminous matter [2].

As people continued to study dynamical data from our own and the remote galaxies, more data supporting the existence of dark matter came out. With the advance of technology, acquisition

of high-resolution optical spectrum from remote galaxies became possible. In the 1980s, Vera C. Rubin and her co-workers studied data from 60 spiral galaxies with different morphological type and luminosities [3]. They researched how the velocity of gas clouds changes with distance from the center of the galaxy. From Newton's law of universal gravitation, the velocity is $\nu \sim \sqrt{\frac{m(r)}{r}}$, here r is the distance from the center, and the $m(r)$ is the total mass enclosed in the sphere with radius r. If all the mass is distributed in the luminous central area, the velocities should decrease in the edge of the galaxy. However, they found that the velocity curves stay flat at a large distance, which indicates the existence of dark matter. Some of their rotation curves are shown in Figure 1.1. Their work not only gave evidence of dark matter but also suggested that dark matter is clumped around galaxies instead of uniform everywhere.

1.1.2 Baryonic Candidates

The missing matter problem has two possible solutions: 1, Newton's law of universal gravitation needs to be modified at large scale; 2, dark matter, either baryonic or non-baryonic, makes up a large part of the universe.

- Modified Newtonian dynamics (MOND) was proposed by Mordehai Milgrom in 1983 [4]. The core of this theory is Milgrom's law which modified Newton's second law:

$$F_N = m\mu\left(\frac{a}{a_0}\right)a \quad \text{where} \quad \mu\left(\frac{a}{a_0}\right) = \sqrt{\frac{1}{1+\left(\frac{a_0}{a}\right)^2}}$$

  At a low acceleration, it deviates from Newtonian dynamics and can explain the flat curve at large distance. However, MOND still requires the existence of dark matter, though way less than the requirement of standard Newtonian dynamics. Furthermore, in 2006 the observation of the "Bullet Cluster" showed that the center of missing mass is quite offset from visible mass [5]. This is strong evidence for the matter explanation.

- Neutron stars, black holes, brown and white dwarfs only emit little or no light. They are categorized as massive astrophysical compact halo object (MACHO). Very naturally, it was

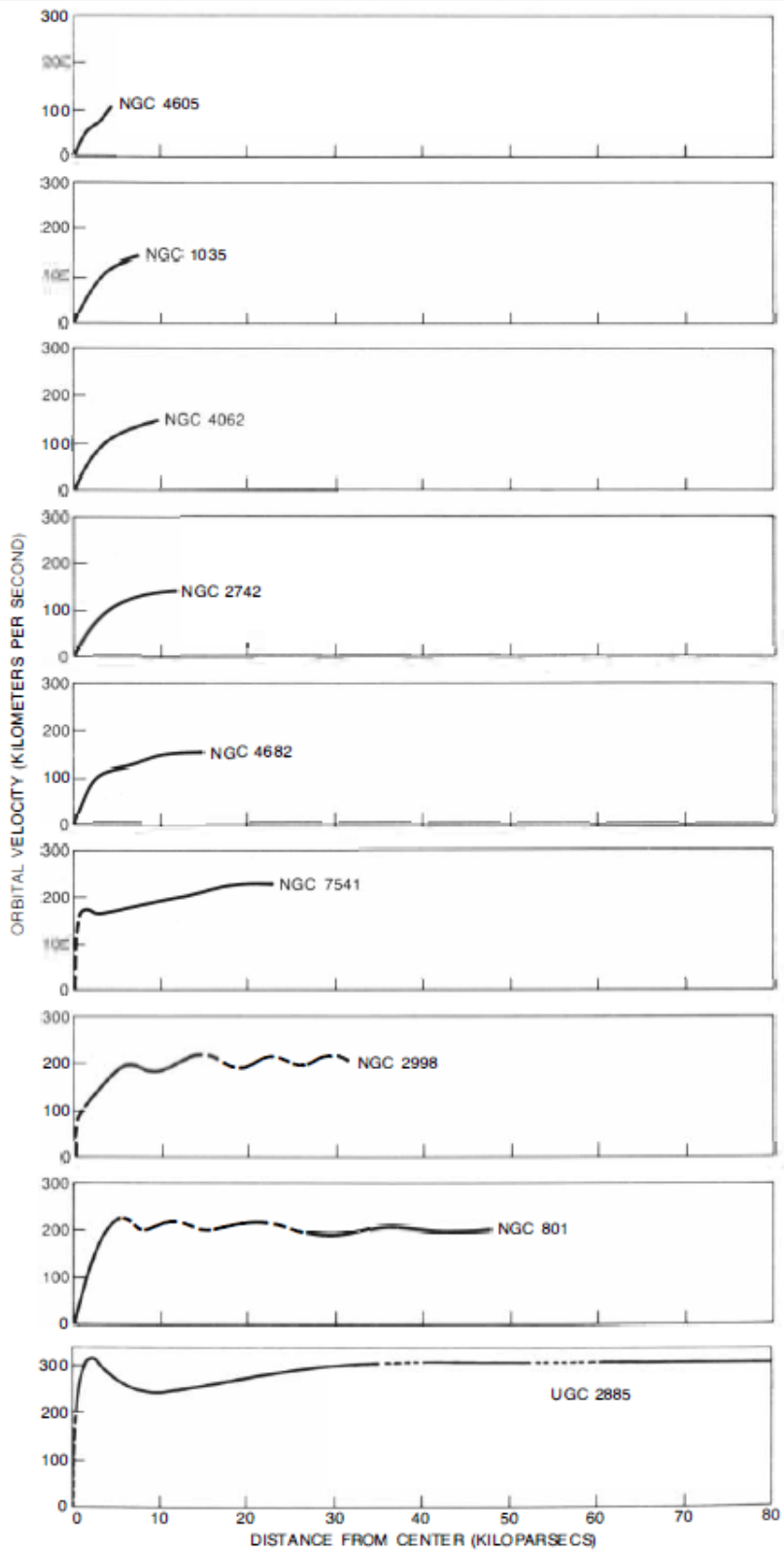

Figure 1.1: Rotation curves of three Sc galaxies. It shows the orbital velocity as a function of the distance from the center of a galaxy. At large distance, the curve is flat. Reprinted with permission from [3].

one of the earliest proposed candidates for dark matter. Although no light from them can be observed on the earth, we can search for gravitational microlensing which would indicate the existence of MACHOs. Several collaborations, like the MACHO Collaboration [6] and the EROS-2 Survey [7], searched for MACHOs in the Milky Way halo. However, the number of MACHOs they observed is too small to count for a non-trivial part of the total dark matter mass.

1.1.3 Non-Baryonic Candidates

As many efforts to search for baryonic dark matter failed, new cosmological evidences showed at least a majority of dark matter should be non-baryonic.

When people study the development of the universe, several things lead them to non-baryonic dark matter. The ratio of deuterium to hydrogen in the distant area, which is related to the baryonic density, the variation in cosmic microwave background (CMB) and the distribution of galaxies density in the universe, all can be used to estimate the ratio of baryonic matter to total matter in the universe. Even better, results from each method agree quite precisely. It shows the composition of all matter in our universe in Figure 1.2.

Weakly interacting massive particles (WIMPs) are one of the most popular dark matter candidates, partially because of the coincidence known as "WIMP miracle". Hypothetically, WIMPs were created thermally in the early universe. As the universe was cooling down, the number of WIMPs is decreasing due to self-annihilation. On the other hand, the universe is expanding, and at some point, the WIMP gas got so dilute that the chance they can find each other to annihilate is very low. This is called the freeze-out. The statistical calculations showed that if we assume the self-annihilation cross section of WIMPs is the same as that of the electroweak force, the thermal relic density of WIMPs will be equal to the current dark matter density. This process did not include a hard constraint on the mass of a single WIMP particle, which could range from the order of GeV to the order of TeV [9].

Alternatively, axion is another candidate. The concept of axion was originally created to solve the strong-CP problem, but it turned out to be a promising candidate for dark matter as well.

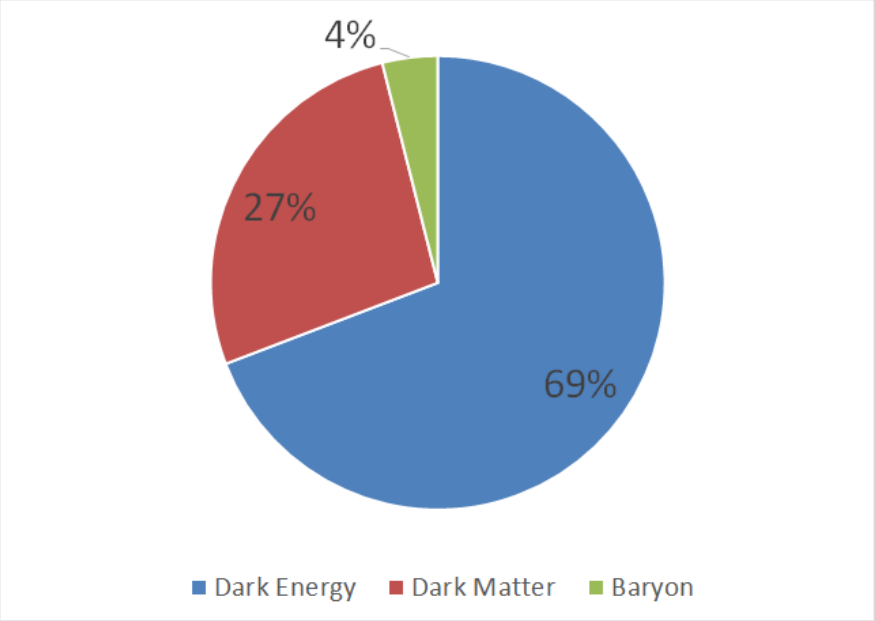

Figure 1.2: This data comes from [8].

Axion can satisfy two requirements as a dark matter candidate: 1, the population of axions have a sufficient quantity to count for the required dark matter energy density. 2, they do not or only weakly interact with conventional matter. Like other candidates, the existence of the axion can solve both fundamental particle physics problem and the dark matter puzzle. The mass of an axion ranges from the order of peV to the order of meV [9].

There are many other candidates which cover a very wide range in mass. The ways to search for the dark matter fall into three categories: direct detection, indirect detection and production in colliders. Indirect detection uses various ways to detect the annihilation or decay products of dark matter. Direct detection, on the other hand, detects the elastic scattering of dark matter particles off the target nuclei. Here we will focus on the direct detection of WIMP.

1.2 Direct Detection

Direct detection relies on the interaction of dark matter and the target nucleus in detectors. The differential WIMP-nucleus scattering cross section includes two parts: spin-independent (SI) term and spin-dependent (SD) term.

Since the de Broglie wavelength of the WIMP is large, it interacts with the target nucleus coherently. The SI term, as a result, is related to the atomic mass of the target nucleus, $\sigma_{SI} \sim A^2$. A heavier atom can lead to a larger cross section. The SD term σ_{SD}, on the other hand, primarily depends on the nuclear spin of the target nucleus.

Since 1987, many experiments have been conducted to directly search for dark matter, either focus on SI interaction or sensitive to SD interaction. Some of these projects and the target material are listed in Table 1.1.

Figure 1.3 shows the exclusion limit plot for the WIMP search, The bottom shaded part is the neutrino floor, a region at which most experiments are not able to tell the difference between a WIMP signal and a coherent neutrino scattering. These neutrinos mainly come from the Sun and atmosphere.

Some of the projects are more sensitive in higher mass ranges while others have a bigger advantage in the lower mass range. However, each curve for a specific experiment does share a similar shape.

In the lower mass range (below 10 GeV), the sensitivity is getting worse quickly. In the higher mass range (above 100 GeV), the sensitivity is not good either. A simplified explanation for this behavior is provided here.

In its simplest form, the energy spectrum of the scattering event rate can be given by:

$$\frac{dR}{dE_R} = \frac{R_0}{E_0 r} exp(-\frac{E_R}{E_0 r}), \quad where \quad r = \frac{4M_T M_D}{(M_T + M_D)^2} \tag{1.1}$$

Here, R_0 is the total WIMP-nucleus scattering event rate, E_0 is the kinetic energy of the dark matter particle, M_T is the mass of the target nucleus, and M_D is the mass of the dark matter particle. This spectrum is shown in Figure 1.4.

The total event rate,

$$R_0 = \frac{N_0}{A} \times \sigma \times flux, \tag{1.2}$$

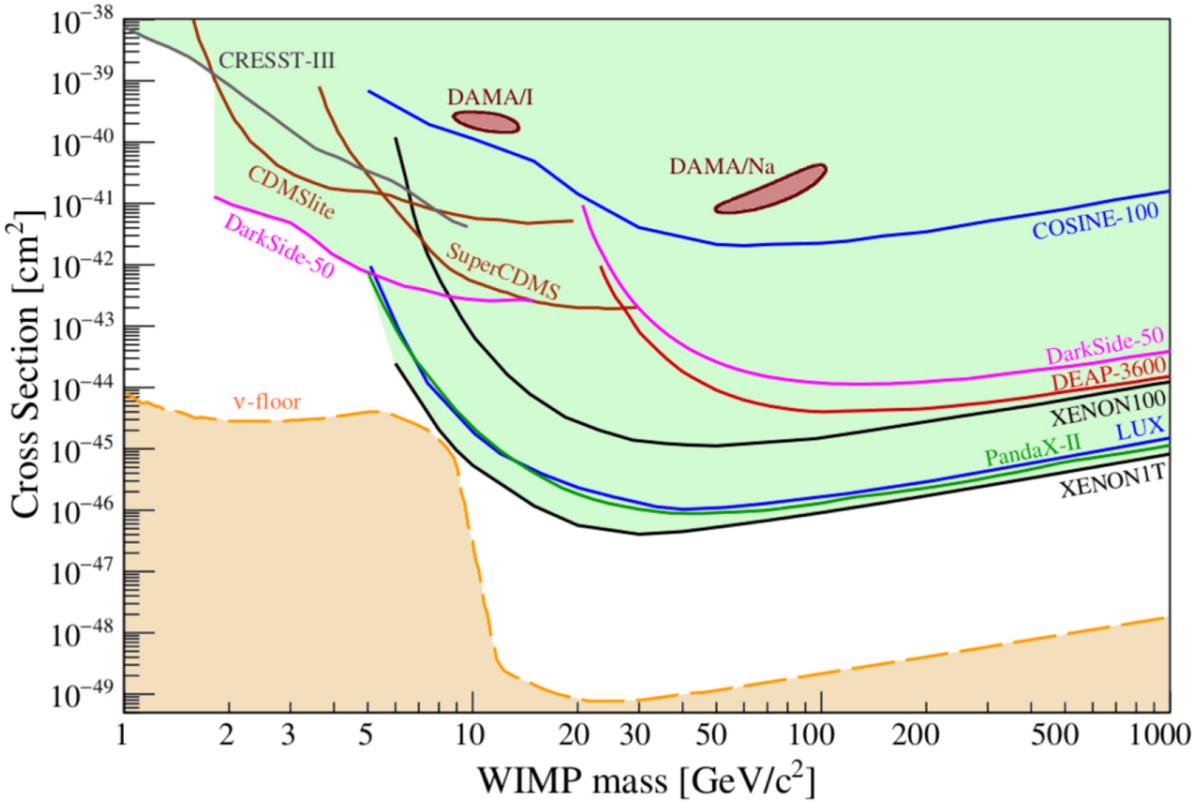

Figure 1.3: Experimental parameter space for various projects searching for WIMPs. It is for spin-independent interaction. The region above a line is excluded from WIMP candidates, as the result of the experiment the line represents. The yellow region on the bottom part is the neutrino floor which is the ultimate background. Reprinted with permission from [10].

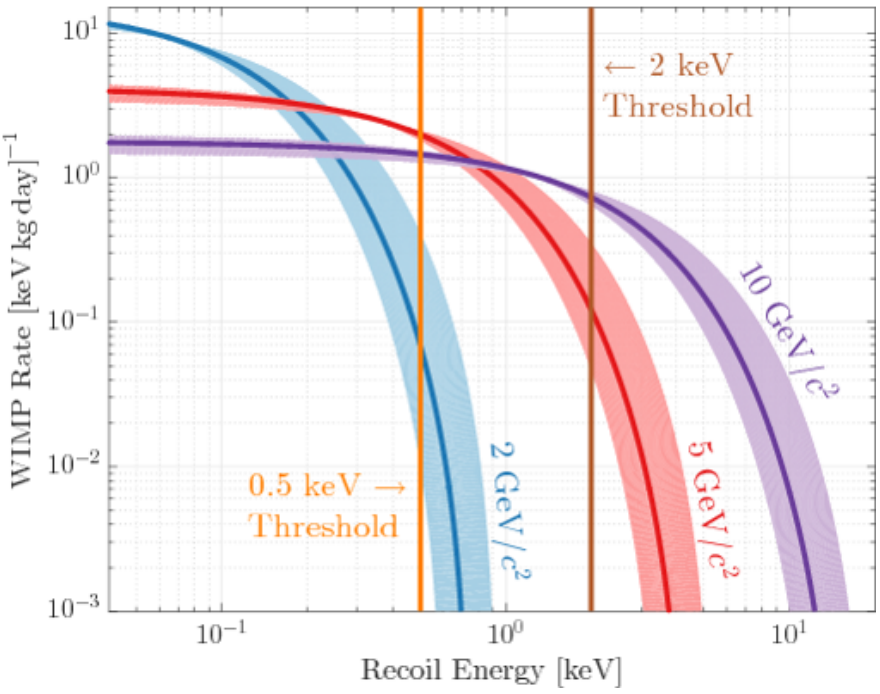

Figure 1.4: The differential events rate for different WIMP masses. Reprinted with permission from [11].

is proportional to the cross section σ, the number of target atoms N_0, and the flux of the dark matter at the detector's location.

A particle detector can only trigger when the recoil energy E_R is above the energy threshold. The event rate caught by the detector is

$$R = R_0 \times \int_{E_{threshold}}^{E_{max}} \frac{1}{E_0 r} exp(-\frac{E_R}{E_0 r}) \tag{1.3}$$

From Section 1.1, the total mass of the dark matter particle is a constant. If the mass of a single dark matter particle is large, the number of them would be small so is the flux. For the same detector, it requires a bigger cross section to see an interaction event, according to Equation 1.2. This can explain the worse sensitivity in the higher mass range.

In the lower mass range, the recoil energies of a majority of events fall below the threshold. In this case, the integral in Equation 1.3 is small, so it requires more total events R_0 to detect an interaction, which corresponds to a bigger cross section limit, according to Equation 1.2. As a

result, it needs a low threshold detector to explore the low mass range.

1.2.1 Background

To search for very rare WIMP scattering events, it is necessary to have a low background environment. The background can be classified into two categories: electron-recoil background and nuclear-recoil background.

WIMP does not carry any charge, so it is very unlikely to scatter on electrons. All electron-recoils thus are considered background noise. γ rays and β particles are the main sources for the electron-recoil background, which can be shielded by lead, copper or a lot of water. Many detectors have a specific mechanism to discriminate electron-recoils from nuclear-recoils.

Nuclear-recoils from neutrons leave the same signals like those from WIMPs, it is almost impossible to distinguish between them except the case when the detector size is large enough to allow neutrons scattering multiple times within the detector. Shielding is the best way to avoid this. Polyethylene, paraffin, or water can efficiently moderate neutrons. Many dark matter search experiments are set up deep underground to reduce neutrons induced by muons.

A lot of other efforts can be made to reduce background: active veto, careful selection of material, target purification, etc. The goal is to realize an almost zero background in the region of interest.

1.2.2 Current Experiments

Many kinds of material have been used as detectors due to their specific properties.

Cryogenic detectors like germanium and silicon are the first kind to search for dark matter. CDMS [12] and SuperCDMS [13] are examples which chose high purity germanium and silicon as their target material. Cryogenic detectors are operated at very low temperatures (often $\leq$ 50 mK) to reduce electronic noise. A WIMP scattering will increase the temperature of the detector slightly which can be detected by a transition edge sensors (TES). The advantages of cryogenic detectors include excellent energy resolution, low threshold, and the ability to reject electron recoils effectively when both phonon and ionization signals are collected. However, it needs to be

Experiment	Type	Target	Mass [kg]	Laboratory
CDEX-10	Crystal	Ge	10	CJPL
CDMSLite	Cryogenic	Ge	1.4	Soudan
COSINE-100	Crystal	NaI	106	YangYang
CRESST-II	Cryogenic	$CaWO_4$	5	LNGS
CRESST*	Cryogenic	Al_2O_3	5×10^{-4}	above ground
DAMA/LIBRA-II	Crystal	NaI	250	LNGS
DarkSide-50	TPC	Ar	46	LNGS
DEAP-3600	Single phase	Ar	3300	SNOLAB
DRIFT-II	Directional	CF_4	0.14	Boulby
EDELWEISS	Cryogenic	Ge	20	LSM
LUX	TPC	Xe	250	SURF
NEWS-G	Gas Counter	Ne	0.283	SNOLAB
PandaX-II	TPC	Xe	580	CJPL
PICASSO	Superheated Droplet	C_4F_{10}	3.0	SNOLAB
PICO-60	Bubble Chamber	C_3F_8	52	SNOLAB
SENSEI*	CCD	Si	9.5×10^{-5}	FNAL
SuperCDMS*	Cryogenic	Si	9.3×10^{-4}	above ground
XENON100	TPC	Xe	62	LNGS
XENON1T	TPC	Xe	1995	LNGS
XMASS	Single phase	Xe	832	Kamioka

Table 1.1: List of old, current and future project searching for WIMPs with different kinds of materials. Reprinted with permission from [10].

operated at extremely low temperature (mK) which can be challenging and costly. It can also be difficult and expensive to increase detector mass.

Noble gases like argon and xenon are another popular option since they can easily produce photon and charge signals. Detector with noble gas could either work in single phase mode, when only scintillations are detected, or dual phase mode, with both scintillation and charge signals so as to provide nuclear/electron recoil discrimination. In most cases argon or xenon is liquefied and put in a time projection chamber (TPC), signals are read out by photomultiplier tubes. Experiments like LUX [14] and XENON1T [15] use a large amount of xenon and are sensitive in the high mass range but struggle in the lower mass range as shown in Figure 1.3.

Since the magnetic bubble chamber resembles the traditional bubble chamber in many aspects, I will discuss more detail about it.

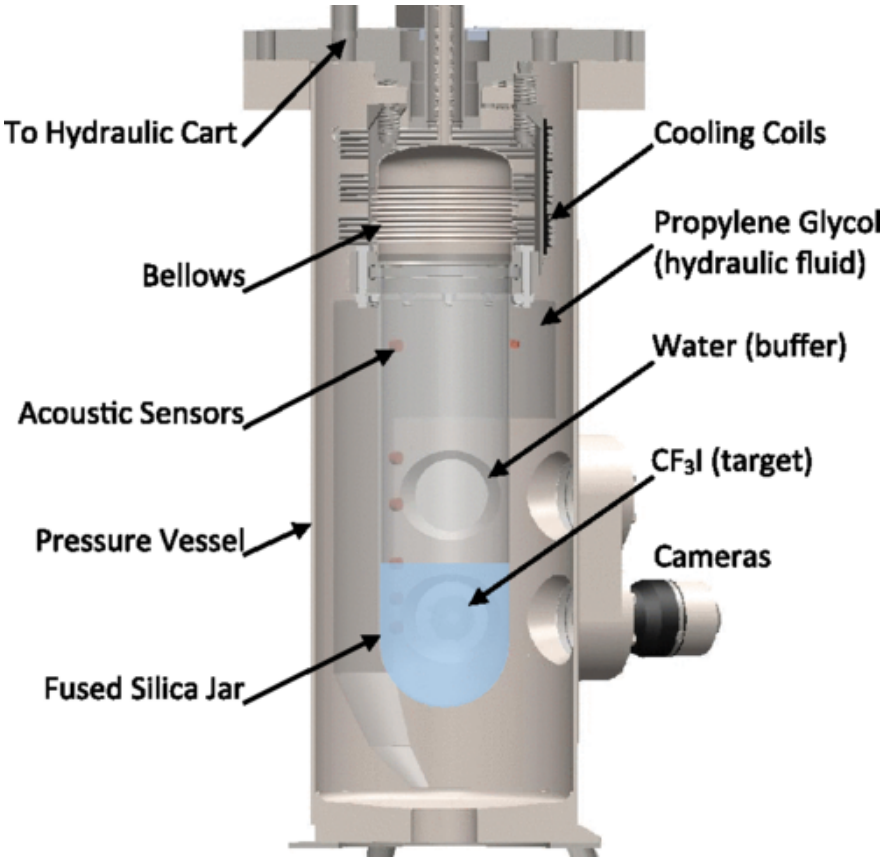

Figure 1.5: A schematic of the PICO-60 bubble chamber. The energy threshold is 7 to 30 keV. Reprinted with permission from [17].

1.3 Bubble Chamber

The bubble chamber was invented in 1952 by Donald A. Glaser. The basic idea is to place a certain kind of liquid just below its boiling temperature. When a particle scattering deposits some energy to a small local area in the superheated liquid, a small amount of the liquid will evaporate to gas and forms a bubble. A camera can record this event.

Right now this technology is used in the WIMP search, for example by the PICO collaboration using the material C_3F_8 and CF_3I [16, 17]. The equipment to operate this detector is sketched in Figure 1.5 . Some of the advantages of the bubble chamber are:

1. The isotope ^{19}F in C_3F_8 has the highest sensitivity for spin-dependent WIMP-proton coupling, this helps the PICO experiment leading the detection of spin-dependent interaction.

2. It can reject electron recoils quite well, since the formation of the bubble relies on the deposited energy density. The electron recoils spreads the energy to a larger area so are less likely to form a bubble. Under proper temperature and pressure, almost all electron-recoils from γ or β rays are excluded.

3. It is easy to set up the experiment with large target mass. The currently deployed PICO-60 has 36.8 kg of CF_3I as target [17], the upcoming PICO-500 can be filled with 1 ton of C_3F_8, which can lead to a very good sensitivity.

4. The bubble chambers used in PICO experiment are operated in a temperature close to the room temperature, it does not require a complicate and expensive cryogenic equipment thus is easier to operate than cryogenic experiments.

5. Easy to get the event location. Cameras are used to take pictures whenever a bubble forms.

On the other hand, a bubble chamber can not measure the value of recoil energy directly, since any recoil energy above the threshold can form a bubble. However, the energy threshold can vary under different temperature and pressure. The recoil energy spectra can be retrieved by ramping the threshold.

The bubble chamber also has a long dead time. Each time when a bubble is formed, or every 2000s without any event, the chamber needs to be compressed for 100s to 600s, which accounts for more than 20% of the total operation time.

As null results continue to be obtained in all of the current experiments, people would like to probe the whole parameter space, especially the big blank area in the lower mass range as shown in Figure 1.3, which requires a low threshold detector.

The magnetic bubble chamber explored in this work has all the advantages of the traditional bubble chamber, but it does not need a long dead time. It also has the potential to achieve a lower energy threshold.

2. SINGLE-MOLECULE MAGNETS MATERIAL AS A PARTICLE DETECTOR

In this chapter, I will discuss some properties of SMM relevant to our project. I will also describe how we can use it as a dark matter detector and why it is a promising technology.

2.1 Properties of SMM

Single-molecule magnet (SMM) was first synthesized in 1980 [18]. The first SMM, Mn12-acetate or $Mn_{12}O_{12}(CH_3COO)_{16}(H_2O)_4$, is still one of the most popular research subjects among more than one hundred kinds of SMMs. $[(C_6H_15N_3)_6Fe_8O_2(OH)_12]Br_7(H_2O)Br \cdot 8H_2O$, abbreviated as Fe_8, is another kind of well known SMM.

Each SMM molecule includes a magnetic core which has an intrinsic magnetic moment and is isolated by some ligands from other molecules. The magnetic core consists of either single or multiple metal atoms. A ligand is a molecule or ion attached to a central metal atom. Because the distance between two adjacent magnetic cores is relatively large, the exchange interaction between them is small. As a result, each core behaves like an independent magnet. That is why this material is called single-molecule magnet.

Different kinds of SMMs may contain different metal atoms or ligands, but they share most of the basic behaviors. Here we will take Mn12-acetate as an example to illustrate some interesting properties of SMM.

2.1.1 Properties of Mn12-Acetate

In Mn12-acetate molecule, the magnetic core consists of 12 manganese atoms and some ligands shown in its molecular formula. The structure of a Mn12-acetate molecule is shown in Figure 2.1.

At sufficiently low temperature, the exchange interaction between the 12 manganese atoms within the magnetic core gives the core a rigid spin of $S = 10$. The effective spin Hamiltonian can be written as

$$\mathcal{H} \approx -DS_z^2 - g_z\mu_B S_z H_z - AS_z^4 + \mathcal{H}' \tag{2.1}$$

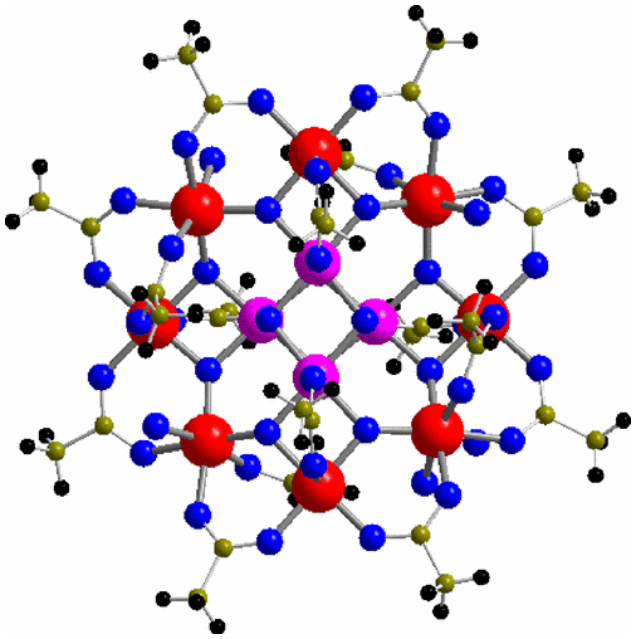

Figure 2.1: Structure of Mn12-acetate viewed along the c axis. Those large red and pink balls are manganese atoms. Reprinted with permission from [19].

Here, the first term creates the anisotropy barrier between spin-up and spin-down states, and the second term is Zeeman energy which breaks the symmetry. When H_z is not zero, the molecules will be in a metastable state as shown in Figure 2.2 [20]. The third term would change the way quantum tunneling works when an external field is applied. The first three terms commute with S_z, so S_z is a conservative quantity without the last term $\mathcal{H}'$. $\mathcal{H}'$ includes all the terms that do not commute with S_z, which leads to quantum tunneling and magnetic avalanche without the need of an external perturbation.

Mn12-acetate crystal is a body-centered tetragonal lattice with only one easy magnetization axis which is almost on the c axis of the crystal. It is tilted a little bit away from the c axis (within $1.7°$). It is simple to find the easy axis by looking at the shape of the synthesized crystal. It is the long side of the crystal shown in Figure 3.11.

Once Mn12-acetate crystals are magnetized, there are two ways it can overcome the potential barrier to relax the magnetization: thermal activation and quantum tunneling. If the temperature is sufficiently low, the thermal activation rate becomes very low and the dominant relaxation mecha-

nism is quantum tunneling or thermal assisted tunneling.

A very important point for our project is that at low temperatures, especially below its blocking temperature (about 3 K), the relaxation process is very slow. It remains slow even when an external field anti-parallel to the magnetization direction is applied, as long as there is no resonant quantum tunneling (which will be discussed in detail in Section 2.1.2). So the magnetization can be stable for a very long time (months or even years). This is crucial for searching rare events from interactions like dark matter scatterings.

2.1.2 Resonant Quantum Tunneling

When it is below its blocking temperature, Mn12-acetate exhibits a hysteresis curve when an external magnetic field is scanned, as shown in Figure 2.3. In this curve, the relaxation is much faster at certain magnetic field [21]. The whole curve displays a step shape. The reason for that is the resonant quantum tunneling. When the field was increased, as shown in Figure 2.2, one of the two energy wells is raised and the other is lowered. To some point, one level $|-a\rangle$ in the left well will be aligned to another level $|b\rangle$ in the right well. When this happens, the quantum tunneling is in a resonant mode and the relaxation speed is much faster. Note that $a \neq b$.

Without the S_z^4 term in the Hamiltonian, all levels would be aligned at the same time. S_z^4 term breaks this coincidence and each level will be matched in different values of the field.

There is one more interesting fact about SMM. After an SMM crystal is magnetized, we can add an external magnetic field anti-parallel to the magnetization direction and increase the field slowly from zero. Before the field reaches the first value for resonant quantum tunneling, the relaxation is actually smaller than when the field is zero. That is because levels in the two potential wells are mismatched and tunneling is suppressed [22].

2.1.3 Magnetic Avalanche

At low temperatures, a single molecule needs to go through a slow relaxation process by either thermal activation or tunneling. On the other hand, the magnetization of an Mn12-acetate crystal can go through an abrupt change. This phenomenon is called magnetic avalanche and this is the

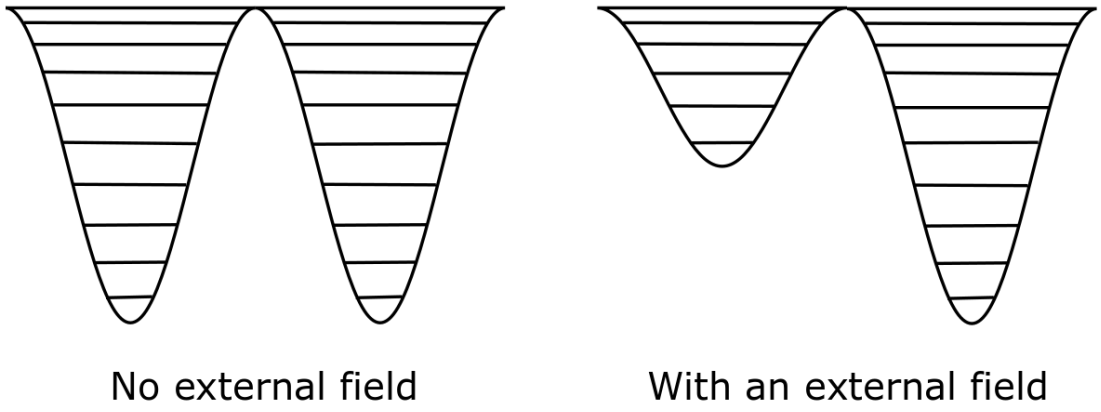

Figure 2.2: Double well potential for single molecule in Mn12-acetate. The left one is the case without external magnetic field and the right one is with external field on.

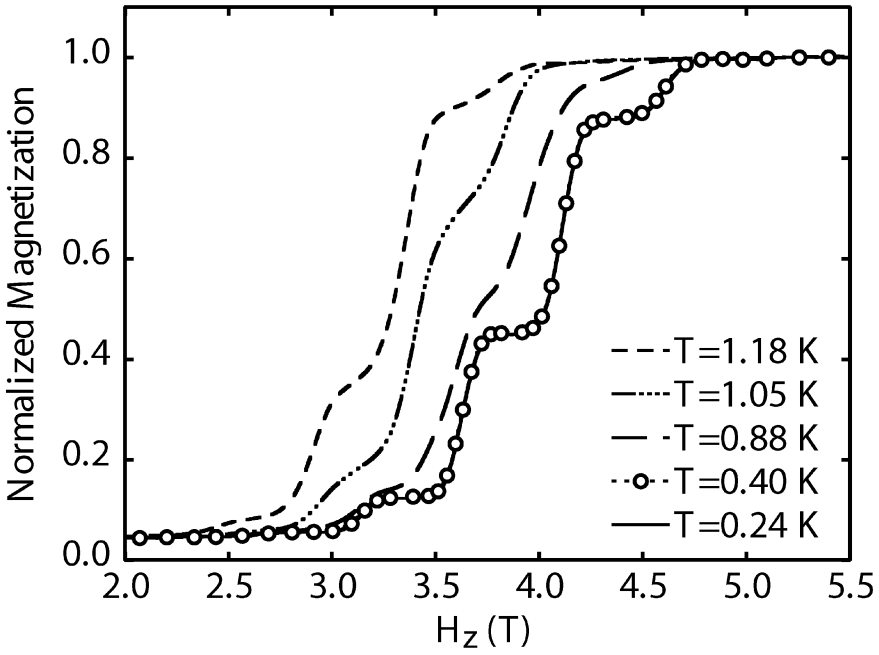

Figure 2.3: Hysteresis curve for Mn12-acetate in different temperatures. Those steep steps are due to resonant quantum tunneling. Reprinted with permission from [21].

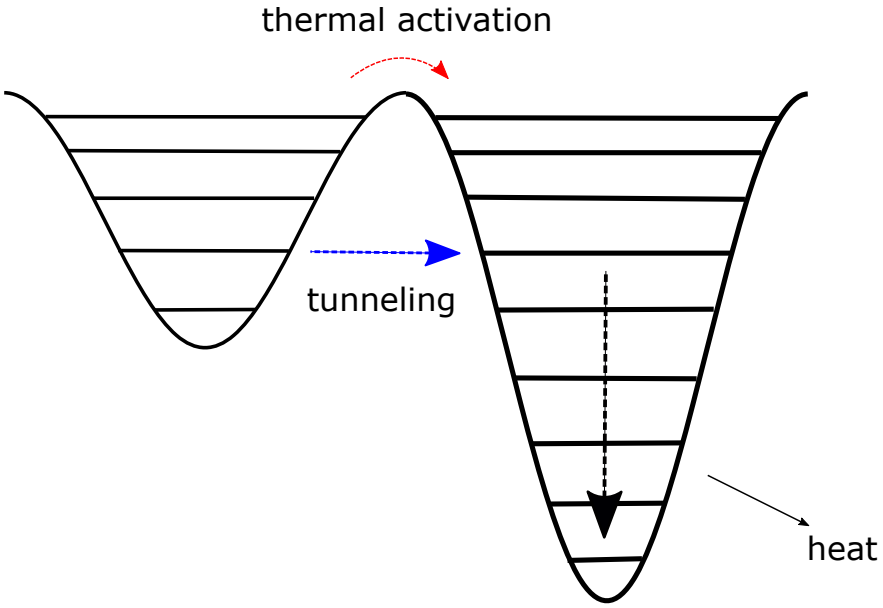

Figure 2.4: Mangetic avalanche dynamics

main reason it can be used as a particle detector.

The way magnetic avalanche works is illustrated in Figure 2.4. When one or more molecules in the left well get flipped, i.e., they jump to one of the excitation states in the right well either by thermal activation or tunneling, and they will relax to the ground state afterward. Zeeman energy is released in this process and turns into heat, which warms up the surrounding area. If the environment temperature and magnetic field are tuned to the right value, this heat can make the surrounding molecules relax quickly and release more energy to warm up and relax more molecules until the magnetization of the whole crystal is flipped and aligns with the direction of the external field.

Magnetic avalanches propagate at the speed of about 10 m/s. For the size of the crystals we used, the avalanches will finish quickly. As shown in Figure 2.5, the whole process of an avalanche took about 0.2 ms [23]. Also note that the dimension of the Mn12 crystal used in the Figure 2.5 is $1.5 \times 0.3 \times 0.3\ mm^3$, and the change in the magnetic field on the surface of the crystal is in hundreds of Gauss, which can be easily picked up by a commercial cryogenic Hall sensor.

When a magnetic avalanche happens, three kinds of signals are generated. The first one is the

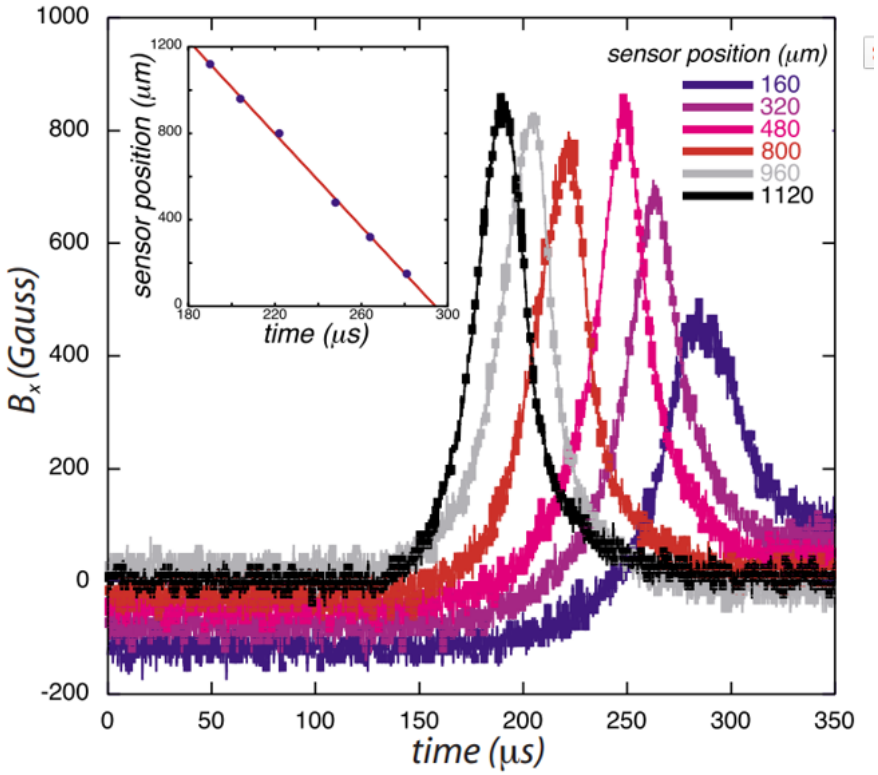

Figure 2.5: Six Hall sensors are attached on different location of the crystal. This figure shows the readings of these sensors as a function of time. Reprinted with permission from [23].

abrupt change in the magnetization. The second one is the change in temperature. Since all the Zeeman energy stored in a crystal is released, the change in temperature can be as large as 2 K. The third one is the radiation emitted in the process of an avalanche. In this project, we only use a Hall sensor to monitor the change in magnetization since it is the easiest and cheapest option, but other options like temperature change and radiation are available for future development.

2.2 SMM as a Particle Detector

Recently there was a proposal to utilize magnetic avalanche to create a new way for dark matter detection in the mass range of $10^{-3}\ eV$ to 10 eV [24], the following discussion is mostly based on that paper. This detection technique was named as magnetic bubble chamber since the way it works resembles the mechanism of the traditional bubble chamber. The general idea is shown in Figure 2.6.

A set of SMM crystals are magnetically polarized in a cryogenic fridge. Then they are cooled down below their blocking temperature (normally below 3 K). The magnetization of these crystals can survive in an external magnetic field anti-parallel to the magnetization for a long time. When they are in this metastable state, if an incoming particle (WIMP, for example) recoils off a nucleus, the temperature within the small area close to the nucleus will increase. If the change of the temperature is big enough, several molecules nearby might be relaxed. In this case, Zeeman energy will be released and heat up a larger surrounding area, thus more molecules will be flipped which will release even more Zeeman energy. In this thermal runaway process, all the spins in one crystal would change to the opposite direction and we can check the change in magnetization to catch the signal.

So far, no experiment is capable of detecting the WIMP signals within the mass range of 1 GeV to 1 TeV. Theoretically, the mass of WIMP particles could range from 10^{-3} eV to 100 MeV. SMM crystals, when used as a magnetic bubble chamber, can possiblely detect WIMP particles in this range. As a dark matter detector, several aspects, like threshold, stability and background rejection, need to be discussed.

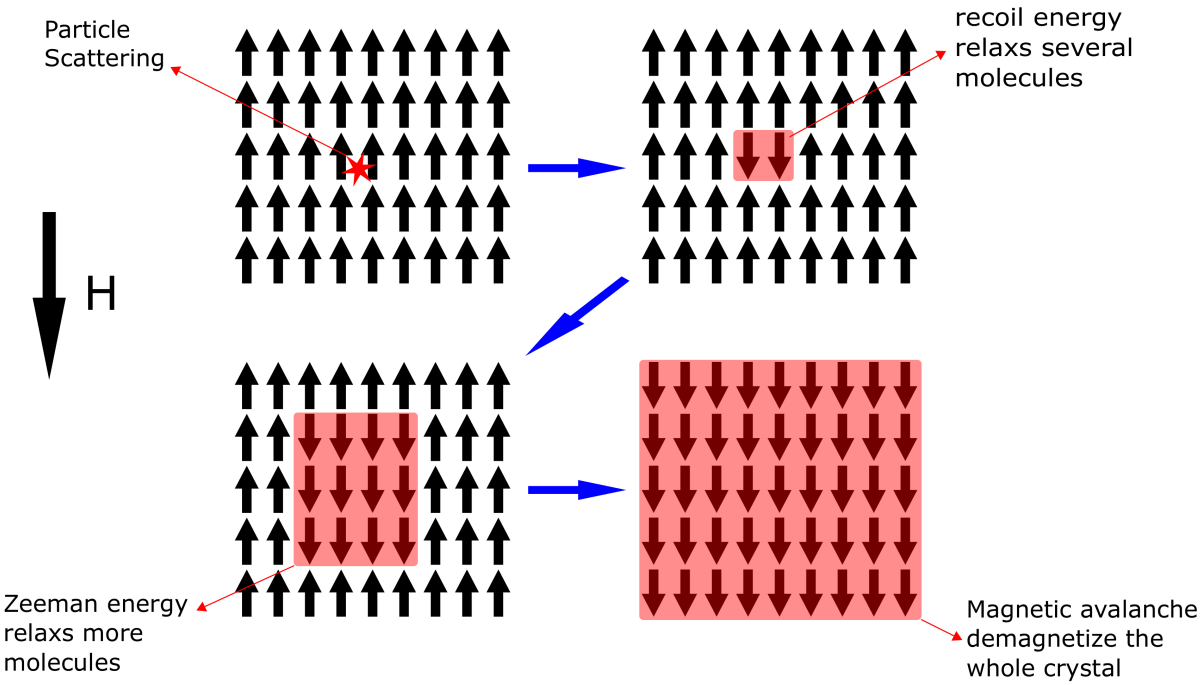

Figure 2.6: Some single-molecule magnet crystals are polarized at first. The magnetic field is then reversed to the opposite direction. The Energy deposited by a particle scattering in a crystal causes localized heating which relaxes some spins, releasing the stored Zeeman energy. The released Zeeman energy will relax more nearby spins, releasing more energy and triggering a magnetic avalanche in the crystal.

2.2.1 Energy Threshold

In this section, I will briefly talk about how to estimate the energy threshold of a magnetic bubble chamber, following the paper [24].

To trigger a magnetic avalanche, how fast the magnetic cores can relax is important. At low temperatures, the relaxation process is dominated by tunneling. Whereas at higher temperature, it is the thermal activation determining the relaxation time. After a scattering, the recoil energy will warm up a small area. Within this area, the temperature is high. The relaxation time relates to the thermal activation is given by:

$$\tau = \tau_0 exp(\tilde{U}(B)/kT) \tag{2.2}$$

After the recoil energy E_0 is deposited in a small area, it will increase the local temperature. To trigger magnetic avalanche, the molecules in this area need to be relaxed before the deposited heat dissipates to other nearby areas. Assuming the size of this area is R, it can be shown the condition to trigger avalanche is [24]:

$$E_0 \gtrsim \frac{c_0 R^3 (U - 1/2 \triangle E_{Zee})^4}{ln[\frac{R^2}{\tau_0 \alpha}]^4} - \rho_S R^3 \triangle E_{Zee} \tag{2.3}$$

where c_0 is the volume-specific heat capacity, U is the potential barrier at zero magnetic field, $\triangle E_{Zee}$ is the Zeeman energy, τ_0 is the relaxation time contant in Equation 2.2, α is the thermal conductivity and ρ_S is molecule density. This E_0 sets the energy threshold of a magnetic bubble chamber, i.e., the minimum recoil energy required to trigger a magnetic avalanche.

Parameters of some SMM material is shown in Table 2.1. In this table, three parameters are listed: J, τ_0 and U, since they vary significantly for different kind of SMMs. By choosing proper range of these three parameters, we can get the energy threshold in the desired range.

The Zeeman energy can be tuned by changing the external magnetic field, while the temperature limits how big the anti-parallel field could go without destroying the stability. In short, after choosing a specific kind of SMM, we can also change the value of temperature and field to further

SMM	J	τ_0[s]	U[K]
Mononuclear Transition Metal SMMs $[K(2.2.2-\text{crypt})][\mathbf{Fe}(C(SiMe_3)_3)_2]$	7/2	4.5×10^{-10}	354
Multinuclear Transition Metal SMMs			
$\mathbf{Mn}_{12}O_{12}(O_2CCH_3)_{16}(H_2O)_4 \cdot HO_2CCH_3 \cdot 4H_2O$	10	2.1×10^{-7}	61
$\mathbf{Mn}_{12}O_{12}(O_2CC_6H_4\text{-}p\text{-Me})_{16}(H_2O)_4 \cdot HO_2CC_6H_4\text{-}p\text{-Me}$	10	2.0×10^{-10}	38
$\mathbf{Mn}_{12}O_{12}(O_2CC_6H_4\text{-}p\text{-Me})_{16}(H_2O)_4 \cdot 3H_2O$	10	7.7×10^{-9}	64
$\mathbf{Mn}_6O_2(\text{sao})_6(O_2CPh)_2)_2(MeCN)_2(H_2O)_2$	4	6.6×10^{-8}	24
$\mathbf{Mn}_6O_2(\text{Et-sao})_6(O_2CC(CH_3)_3)_2(EtOH)_5$	6	3.0×10^{-8}	30
$\mathbf{Mn}_6O_2(\text{Et-sao})_6(O_2CC_6H_4(CH_3)_2)_2(EtOH)_6$	12	2.0×10^{-10}	86
$\mathbf{Fe}_4(CH_3C(CH_2O)_3)_2(dpm)_6$	5	2.1×10^{-8}	17
Mononuclear Lanthanide SMMs			
$[\mathbf{Dy}(O^tBu)_2(C_5H_5N)_5][BPh_4]$	15/2	1.2×10^{-12}	1815
Multinuclear Lanthanide SMMs			
$[K(18\text{-crown-}6)][\{[(Me_3Si)_2N]_2(THF)\mathbf{Dy}\}_2(\mu\text{-}\eta^2\text{:}\eta^2\text{-}N_2)]$	29/2	8.0×10^{-9}	178
$[K(18\text{-crown-}6)][\{[(Me_3Si)_2N]_2(THF)\mathbf{Tb}\}_2(\mu-\eta^2\text{:}\eta^2\text{-}N_2)]$	23/2	8.2×10^{-9}	327

Table 2.1: Properties of SMMs for different material. Reprinted with permission from [24].

tune the energy threshold.

2.2.2 Stability

Below its blocking temperature, SMM material can stay magnetized in a reversed external magnetic field for months as long as the field is below a specific limit. This is crucial for WIMP search since we need to run the experiment for a long time to detect rare events. We will try to tune the system so that the external field is a little bit smaller than the value which will break the stability. This will help us to reach a lower energy threshold.

The stability of both Mn12-acetate and Fe_8 crystals were tested in our experiment.

2.2.3 Background Rejection

To trigger an avalanche, it is necessary to warm up the initial area above a certain temperature so that the relaxation time is shorter than the thermal diffusion time. It is crucial that how much the local temperature can increase due to the recoil energy. For nuclear recoil, the deposited energy is confined in a small region because the recoil nucleus is constrained within a crystalline structure which leads to a relatively greater temperature change. On the other hand, if an electron recoil happens, the deposited energy would be distributed to a much larger region since the recoil electron

can wander around the crystal very easily. As a result, the temperature change due to an electron recoil should be smaller than that from a nuclear recoil.

If we tune the trigger condition so that a nuclear recoil can trigger avalanches but an electron recoil can not, this detector will have a good discrimination ability against the electron recoil background.

This strategy can reject gamma and beta background. To minimize the background due to muon or neutrons, shielding will be necessary when the detector is actually running. Some kind of active veto detectors, lead or copper shield and water bricks will be added to surround the detector or the cryostat.

2.2.4 Miscellaneous Advantages and Challenges

Besides the possible low energy threshold and intrinsic electron recoil rejection, the magnetic bubble chamber has some other advantages.

When an incoming particle scatters off the target nucleus elastically, from the conservation of energy and momentum, the maximum recoil energy (when a head-on collision happens) can be given by

$$E_r = \frac{4M_T M_i}{(M_i + M_T)^2} E_i \tag{2.4}$$

where the M_T and M_i are the mass of the target and incoming particles, E_i is the kinetic energy of the incoming particle. From this equation, we prefer to choose a target atom whose mass is similar to the incoming particle. This will maximize the recoil energy for a given incoming particle.

Most SMM molecules include hydrogen atoms. If a dark matter particle has mass of about a GeV or so,, the lightest atom with mass of about 1 GeV can maximize the deposited energy. Small atoms are not sensitive to spin-independent interactions, due to the A^2 dependence, but it is not a problem for spin-dependent interactions. In addition, most kinds of SMM molecules include several heavy atoms, like iron, manganese, dysprosium, so they are also sensitive to spin-independent interactions.

As we discussed in Section 1.3, the traditional bubble chamber is leading the sensitivity for the detection of spin-dependent WIMP-nucleus interaction. The reason is that isotope ^{19}F in either C_3F_8 or CF_3I is very sensitive to spin-dependent interactions. Most SMM molecules have large inherent magnetic moments, so the magnetic bubble chamber is also a good choice to detect spin-dependent interactions.

There are some challenges to use this detector too. First, we lost all the information about the recoil energy except that we know it is bigger than the threshold when we see a signal. To get energy information, we can vary the threshold by controlling the magnetic field and temperature and collect data with different thresholds. Carefully comparison between different sets of data could reveal some energy information, similar to the way traditional bubble chambers work when they are used to search dark matter.

Second, once an avalanche starts, we need to wait for the avalanche to finish, then reset the detector by either removing or reversing the magnetic field. During this time, we can not collect data, which we call as the detector dead time. There are two possible ways to shorten this dead time.

Either we can monitor the magnetization with a very sensitive magnetometer. Once the avalanche is ignited and detected, we remove the external field. The avalanche propagation will stop since there is no Zeeman energy to use anymore. In this way, only a small part of the crystal becomes a dead zone, most part is still active after the field is resumed. Since we do not need to wait for the avalanche propagating through the whole crystal thus the dead time is shorter.

Instead of using a big chunk of crystal, we can also use many small grains with good thermal insulation between them. In this way the avalanche will only propagate within one grain and leave others unaffected, we only get a small dead zone after every event. We do not need to change the external field until the majority of grains become inactive. Another advantage of small grains is they are much easier to synthesize than bigger ones. Even more, if we use small grains, we could identify which grain experienced the avalanche thus get the location information.

Either way, the dead time will be much shorter than the traditional bubble chamber.

2.3 Summary

With the tunable low energy threshold, intrinsic electron recoil rejection, excellent stability, capability to be sensitive to both spin-dependent and spin-independent interactions and other benefits, even with some difficulties, we believe this magnetic bubble chamber is a particle detection technique worth to explore.

3. MAGNETIC BUBBLE CHAMBER EXPERIMENTAL SETUP

Magnetic avalanches in Mn12-acetate have been studied for many years. It is reported that avalanches can be ignited by a heater or surface acoustic waves [23, 25], but it is not yet confirmed that it can be triggered by the scattering of particles. We have designed and conducted an experiment to test this idea.

In this chapter, I will describe how we set up the experiment in detail. At first, I will talk about the equipment. In Section 3.1 I will describe the superconducting magnet. Section 3.2 is about the cryogenic refrigerator. In Section 3.3, I will discuss the way the SMM crystals were prepared. In Section 3.4 I will briefly describe the Hall sensor used in this experiment. I will conclude with Section 3.5 on how everything was put together.

3.1 Superconducting Magnet

In our experiment, we need to add an external magnetic field up to several Tesla to Mn12-acetate crystals. To supply this huge field, superconducting magnet is the best option. Since the Mn12-acetate crystals themselves also require cryogenic environment, we can place the superconducting magnet and crystals in the same refrigerator to operate.

As shown in Figure 3.1, we have a controller and a specific power supply for the superconducting magnet. The controller needs to be turned on before turning on the power supply. The controller controls the current ramping speed, and can be run on a persistent mode to supply a constant current.

The superconducting magnet can only provide field in one direction, so a manual polarity switch is added in the circuit as shown in Figure 3.2 to change the direction of current. The switch is connected to the original circuit with a gauge 6 copper wire to carry large current (up to 80 amps). After this switch is added, resistance across every part of the circuit is carefully checked, especially at the soldered connections. Since the current we are going to use is huge, an unstable connection could cause safety issues and may jeopardize the experiment. It takes a while to operate the switch,

Figure 3.1: Power supply and controller for the superconducting magent

but it serves our purpose well for now. When a real magnetic bubble chamber is developed later on, a programmable and fast switch will be necessary.

The controller has a read out connection. It is connected to a multimeter to read out and record the magnitude of the current (from which the magnetic field can be calculated). The multimeter is further connected through GPIB (General Purpose Interface Bus) to a computer. A proper labview program written for this project can display and record data whenever necessary.

Before using the superconducting magnet, it is important to check the resistance across different parts of the circuit, at both room temperature and the base temperature (below 2K). If the resistances are bigger than expected, the huge current going through the circuit will cause a heating problem.

3.2 Cryogenic Environment

We need to operate the experiment below the SMM's blocking temperature, so it has to be inside a cryogenic refrigerator.

We are using a He3/He4 evaporation refrigerator, as shown in Figure 3.3 and Figure 3.4. There

Figure 3.2: Switch to change direction of magnetic field

is a panel shown in Figure 3.7 to control the gas flow and read pressure at several crucial points inside the refrigerator.

At first, the experiment is set up inside the refrigerator and the superconducting magnet is installed. Thereafter a leak check is performed to make sure the vacuum can is well sealed. The leak check is performed with the leak checker shown in Figure 3.5. It includes two mechanical pumps, one diffusion pump and a mass spectrometer which can even detect a tiny amount of helium-4 or helium-3 gas. It is connected to the vacuum can of the refrigerator, and helium-4 gas is blown to places where it might leak. The reading will tell us if there is a leak. It can also be read out by a labview program to detect a minor leak.

To cool down to 1.5 to 2 K, which is the temperature required for Mn12-acetate crystals, we only need to use helium-4. The basic steps are as follows:

1. Add new lead o-ring and vaccum grease on the edge of the vacuum can to seal the connection, and install the vaccum can;

2. As soon as the vaccum can is installed, we pump it to create a vaccum, which protects Mn12-acetate crystals from moisture. A leak check is then performed;

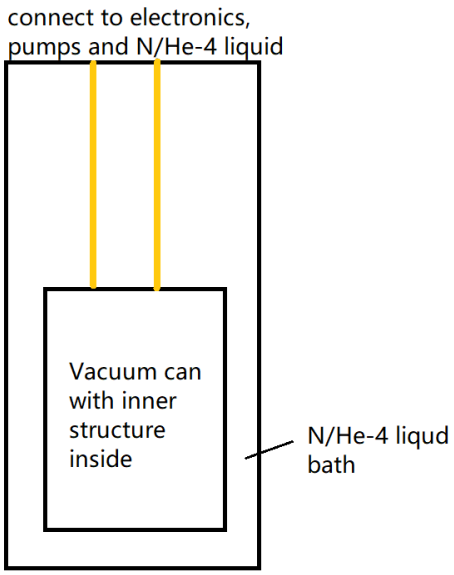

Figure 3.3: Refrigerator structure

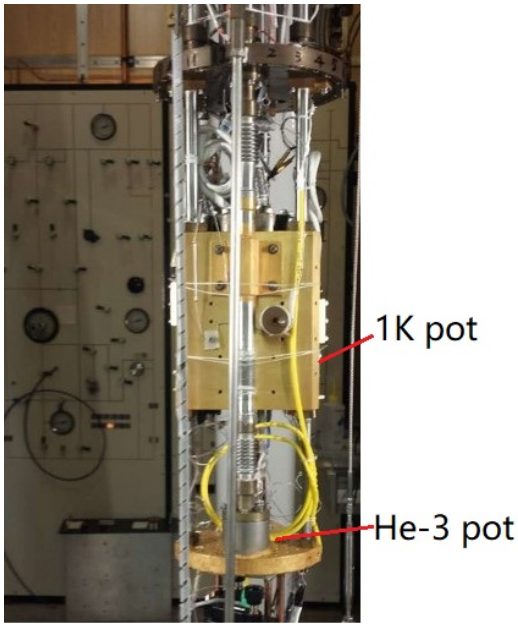

Figure 3.4: Stucture inside the vacuum can

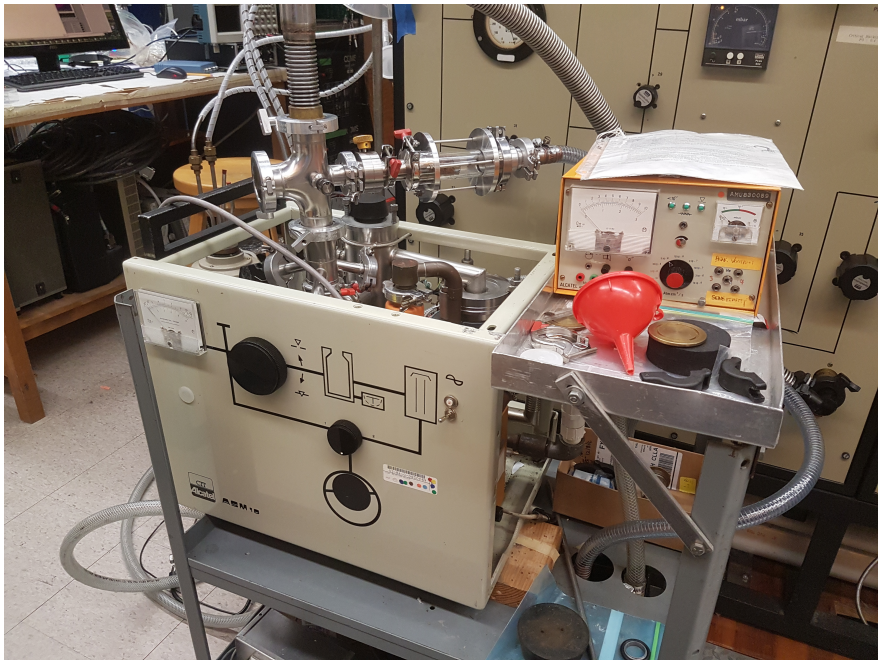

Figure 3.5: Leak checker

Figure 3.6: The refrigerator

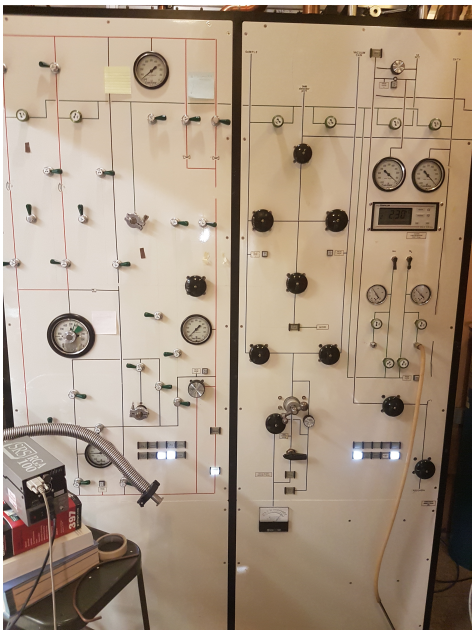

Figure 3.7: Panel to control the flow of gas and read pressure at various positon.

3. Install the superconducting magnet and check all the connections;

4. Install the dewar as shown in Figure 3.6. This completes the installation of the refrigerator. Connect the vaccum can to the leak checker and fill the dewar and 1K pot with helium-4 gas, check if there is any gas leaking from the dewar or the 1K pot to the vacuum can;

5. Fill the vaccum can with either neon or hydrogen gas, which serves as a heat exchange gas. The next step is to transfer liquid nitrogen into the dewar and wait (less than a day) until the temperature reaches about 80 K. If there is no gas inside the vacuum can, the cooling down process will be much slower.

6. Pump the heat exchange gas out of vacuum can and maintain the vacuum so it can stay cold. Push all of the liquid nitrogen out of the bath. Blow some nitrogen gas at room temperature to the dewar and pump it out to take the liquid nitrogen residue out. Repeat it for several times to make sure the dewar is empty.

7. Perform a leak check again at this temperature. The thermal contraction of different parts of

the refrigerator might be slightly different (a screw may shrink more than its hole, etc.), and a new leak can be created during the process of cooling down to the nitrogen temperature (77 K). Below 77K, the dimensions of most materials do not change apparently with the temperature, so it is unlikely that new leak shows up after this step.

8. Connect the liquid helium-4 bottle to the dewar and control the pressure so that helium-4 liquid is slowly transferred into the dewar. The liquid evaporates immediately when it reach the space in the dewar (the bath). The latency would supply the cooling power during this slow transfer. Be sure to add the heat exchange gas back to the vacuum can as soon as the slow transfer starts.

9. The boiling temperature of neon is 27 K at 1 atm. It is 20 K for hydrogen. Before the vacuum can is cooled down to this temperature, the exchange gas needs to be pumped out. We do not want the gas to condensate on the equipment. During slow transfer, if the transfer speed is too high, bottom part of the vacuum can will be cold enough to condensate the exchange gas. To avoid this, the transfer speed needs to be carefully adjusted.

10. Increase the pressure in the helium-4 bottle to speed up the transfer. Now the liquid helium will accumulate within the bath, and we can read the level of the liquid helium from a level detector. The level detector is a metal stick installed inside the dewar, and the part of this stick touching the liquid helium becomes superconductor. By reading the resistance we can know the liquid helium level.

11. Stop the transfer when the dewar is full of liquid helium, and wait for the temperature to drop. When the temperature reaches about 4 K, transfer some He-4 liquid to the 1K pot through two valves (one slow and one fast) connecting the bath and the 1K pot. Turn off the fast valve when there is some liquid in the 1K pot and start the pump connected to it. Soon the temperature will drop below 2 K.

The vapor pressure of a liquid varies with its temperature. Lower is the pressure, lower is the temperature. That is why a pump can cool down the 1K pot. With helium-4, the 1K pot in

our refrigerator can cool the SMM crystals down to 1.5 K. It can not go further because helium-4 becomes superfluid below 2.17 K. When the pump on the 1K pot is working, the 1K pot is colder than the pump line. Superfluid helium will creep up to the warmer pump line where it evaporates. At the warmer spot, the vapor pressure is higher, which limits how low the pressure and the temperature can be in the 1K pot.

To reach a lower temperature, we need to use helium-3. Since it does not become superfluid above 1 mK, it does not have the problem that helium-4 has. Helium-3 is very expensive and hard to get, so it will be circulated in a closed loop, while helium-3 gas will be collected and returned to a helium-3 tank.

Before using Helium-3 circulation, it is good to check the impurities in the tank. Impurities might block the circulation and also indicate a possible leak which needs to be fixed immediately to protect the precious Helium-3.

Helium-3 circulation is illustrated in Figure 3.8. Helium-3 gas goes through a nitrogen trap first (with liquid nitrogen bath at 77 K) to filter most of the impurities. Then it goes through a helium-4 trap (in the bath of the refrigerator) to filter other impurities whose boiling temperature is below 77 K.

Helium-3 gas flows through a capillary which is attached to the 1K pot afterward. The capillary has a high impedance, so the pressure of the gas is raised before feeding into the capillary. The capillary is designed in a way to make sure at this higher pressure, the temperature of the 1K pot is cold enough to condensate helium-3. As liquid helium-3 flows into the He-3 pot, pumping the He-3 pot can further reduce the temperature. In our refrigerator, the temperature has reached as low as 480 mK by far. After the pump, helium-3 gas returns to the tank and starts another circulation.

3.3 Sample Preparation

In this section, I will describe how to prepare SMM crystals for this experiment.

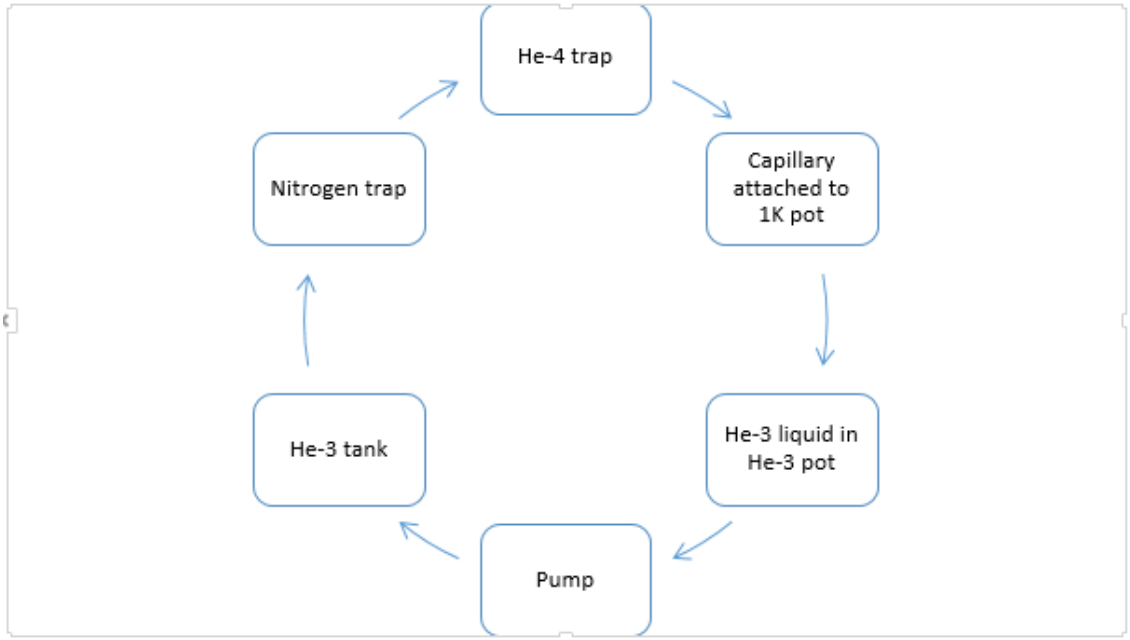

Figure 3.8: Helium-3 circulation

3.3.1 Size and Shape

In this experiment, the main test subjects are Mn12-acetate crystals, as shown in Figure 3.10 and Figure 3.11. The length of the crystals ranges from a little more than 1 mm to about 3 mm, and the width ranges from 0.5 mm to 1 mm.

Some preliminary tests were also done with Fe_8 crystals. The dimension of these crystals are around 1 mm, as shown in Figure 3.9.

3.3.2 Sample Holder

Figure 3.12 shows the sample holder, which is made of oxygen-free high thermal conductivity (OFHC) copper. OFHC copper can transfer heat very quickly, it is also a non-magnetic material and has very low radiation contamination, so it is a good choice for this experiment. The dimension of sample space is 3 mm x 3 mm x 3 mm, and this space could be covered by a plastic cover secured by copper screws.

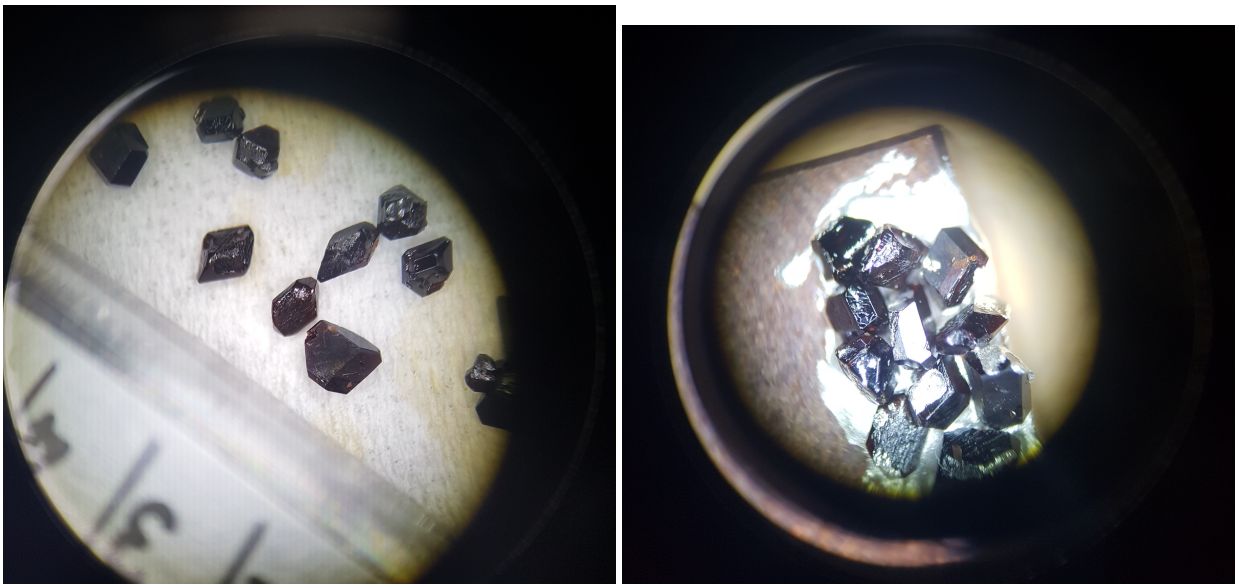

Figure 3.9: Fe_8 crystals under a microscope.

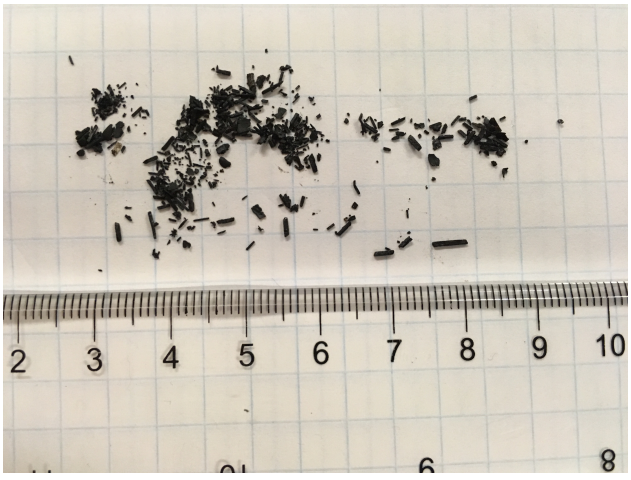

Figure 3.10: Mn12-acetate crystals are synthesized by Phil Bunting from UC Berkeley.

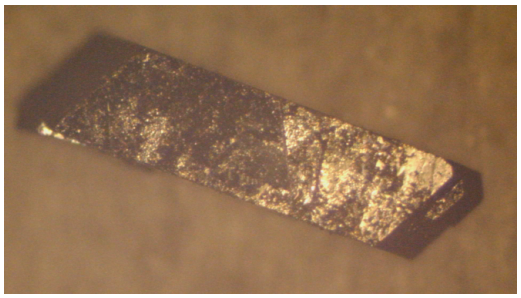

Figure 3.11: Shape of the Mn12-acetate crystal

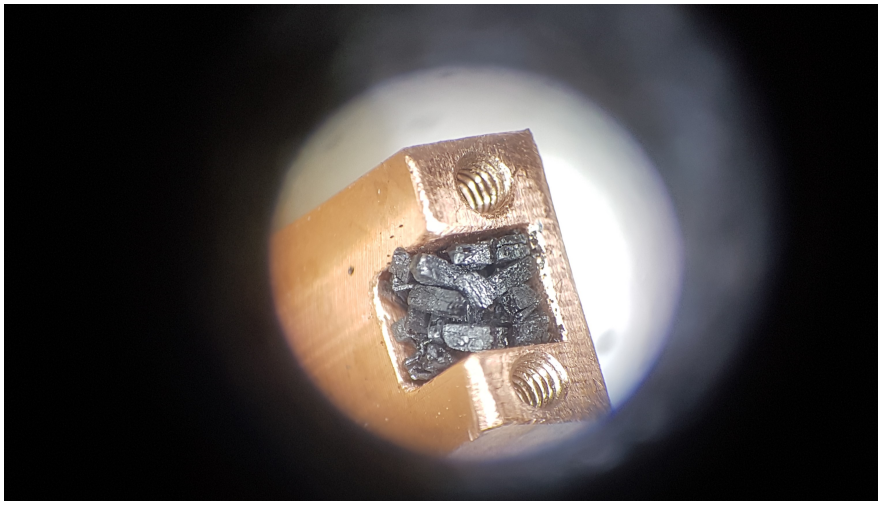

Figure 3.12: OFHC sample holder

3.3.3 Signal Estimate

We are going to use a Hall sensor to detect the change in the magnetic field of the Mn12-acetate crystals. It is useful to estimate the magnitude of the signal before the experiment.

After a magnetic avalanche, all molecules in a crystal will be flipped, as shown in Figure 3.13. Assuming that all spins in the crystal are pointing up before a magnetic avalanche and pointing down afterward, we can estimate how much the reading of the Hall sensor will change by this integration:

$$\delta H = \int_V \frac{1}{4\pi} \left[\frac{3\mathbf{r}(\mathbf{dm} \cdot \mathbf{r})}{r^5} - \frac{\mathbf{dm}}{r^3} \right] \tag{3.1}$$

$$\mathbf{dm} = g_z \mu_B \mathbf{S} dV \rho_S \tag{3.2}$$

where $\mathbf{r}$ is the position vector from an infinitesimal area in the crystal to the active area of the Hall sensor, which is located about 1 mm above the top of the crystal. $\mathbf{S}$ is the spin of one molecule (for Mn12-acetate, $S = 10$). All other variables remain the same as as in Equation 2.1. Given the size of our crystals, a quick analytical calculation gives a signal of about 100 Gauss. Comparing with Figure 2.5, this number is reasonable. The signal is smaller in our case since our Hall sensor is placed 1 mm away whereas it was directly attached to the surface of Mn12-acetate crystals in

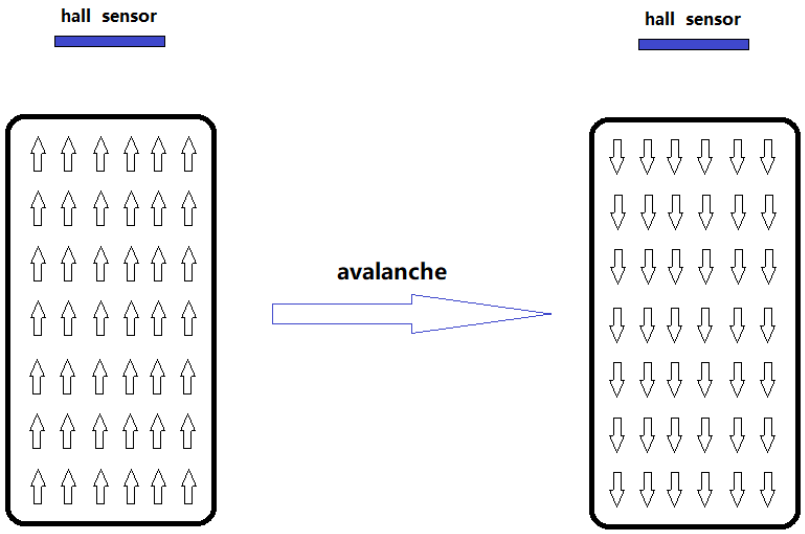

Figure 3.13: All spin in a crystal are inverted after avalanche

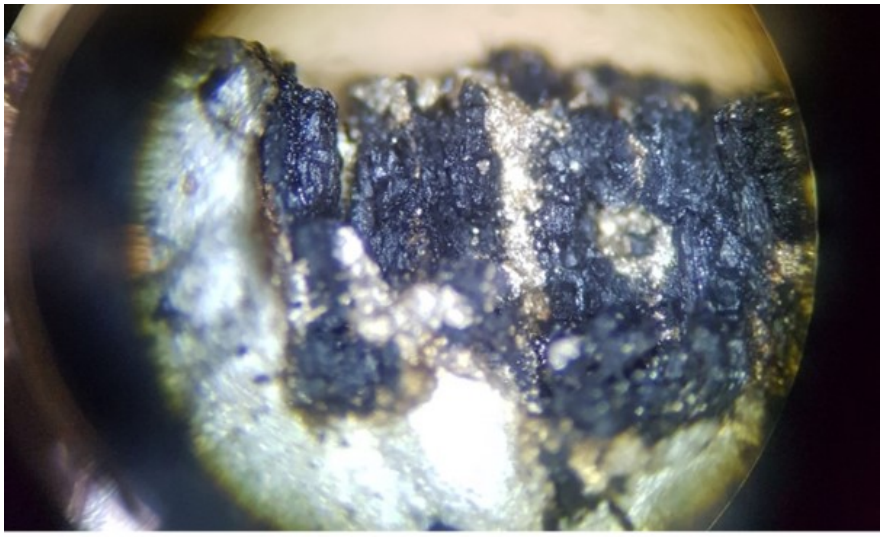

Figure 3.14: Crystals got broken to powder after one run.

the case of Figure 2.5.

3.3.4 Challenges and Solutions

As mentioned in Chapter 2, the longer side of the Mn12-acetate crystal is very close to its easy axis. To maximize the magnetic signal, it is preferred to align all the crystals in a way that the easy axes are on the same direction as the magnetic field of the superconducting magnet. With careful arrangement, they are mostly in the preferred direction with an error up to 10^o.

During the first several runs, some crystals got cracked. Some of them were even broken to powder as shown in Figure 3.14. A few attempts were made to identify the cause of this problem.

1. The first possible cause we explored is thermal expansion and contraction. We cooled the Mn12-acetate crystals from room temperature down to 2 K and warmed them up after each run. The huge temperature change might have destroyed them, since the crystals have different thermal expansion coefficient comparing with the sample holder material. It is also possible that the temperature within the crystal is not uniform in the process of cooling. A warmer part might squeeze a colder part and break it.

   To test our hypothesis, several Mn12-acetate crystals were placed in the sample holder which

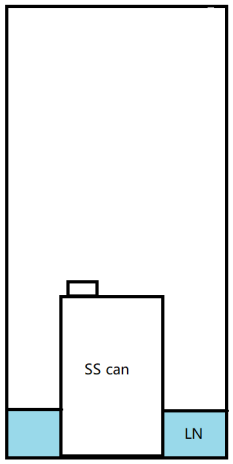

Figure 3.15: Test in liquid nitrogen

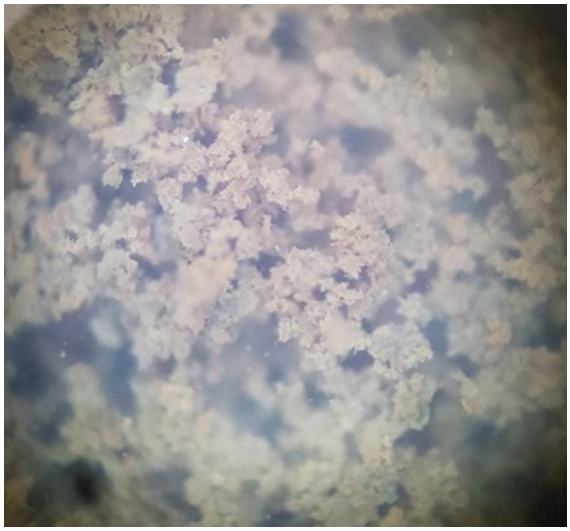

Figure 3.16: Mn12-acetate crystals are dissolved in water

was attached on top of a stainless steel can. The bottom part of the can was slowly submerged into liquid nitrogen as shown in Figure 3.15. The temperature of those crystals slowly dropped to about 80 K, which resembled the situation when we actually run the experiment. The speed of the cooling is quicker in this test though, since the thermal capacity of the stainless steel can is much less than the vacuum can in the refrigerator. In this test, it took between two to three hours to cool down to around 80 K, whereas it took more than 10 hours in the refrigerator. Below 80 K, all materials we used do not shrink much, so we do not need to use liquid helium in this test.

However, several repeated tests show that the crystals remain intact after the tests. So this possible reason was excluded.

2. Another possible reason is the magnetic force which might break the crystals. Because the magnetic field on these crystals was not uniform during the experiment, there would be a pretty big magnetic force exerted on the crystals, trying to drag them to the lower energy spot. Assuming that all the molecules are aligned along the direction of external magnetic

field, calculation shows that for a magnetic field of 1 Tesla,

$$\frac{magnetic\ force}{weight} \approx 29$$

It is clear that this force can move the crystals around within the sample holder and even be able to break the crystals since they are relatively fragile. This also explains the fact that even though all crystals are aligned in the same direction before each run, they are not after the run, as shown in Figure 3.12.

3. During each run, there are moments when the crystals got exposed to air containing moisture which might damage the crystals. One simple test is to dump some crystals in water to see if water could dissolve them. This is found to be true as shown in Figure 3.16. We suspect this to be the most possible reason for the broken crystals.

In later runs, several things were done to protect the crystals.

1. As soon as the vacuum can was installed, the pump connected to it was turned on to keep the crystals in vacuum.

2. Crystals used in the experiment were covered by silver epoxy. The epoxy can transfer heat well and protect crystals from moving by magnetic force or being damaged by water vapor, as shown in Figure 3.17.

3. Crystals were kept in a vacuum box which was located in a dry tent to minimize the chance of them getting in touch with water vapor in the air.

3.4 Magnetometers and Connections

For magnetometers, we chose cryogenic Hall sensors in our experiment since they are affordable and easy to install as compared to SQUID (superconducting quantum interference device). We tested two Hall sensors to make sure they has the required sensitivity. As shown in Figure 3.18, these sensors can clearly tell the difference when the field changes by about 100 Gauss.

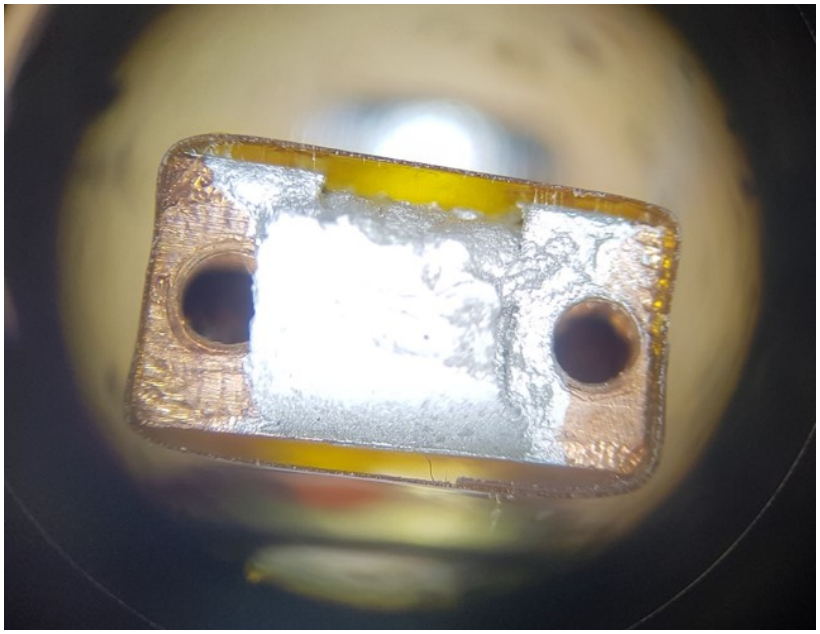

Figure 3.17: Mn12-acetate crystals are protected by silver epoxy.

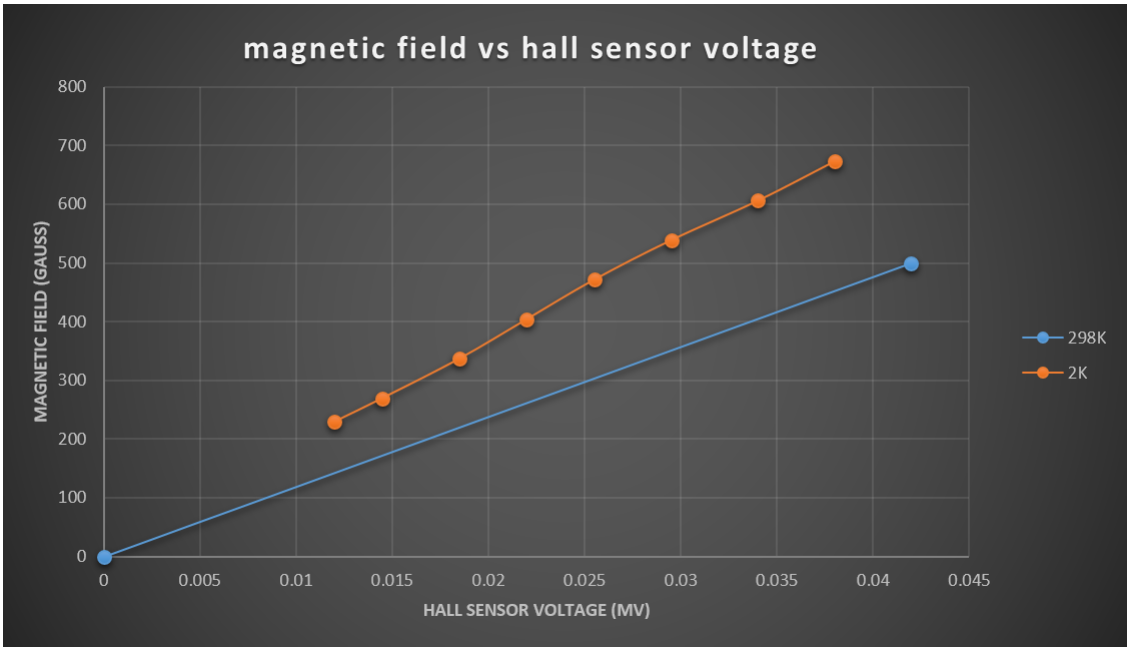

Figure 3.18: Hall sensor sensitivity test

The Hall sensors are connected to a power supply and a multimeter outside of the refrigerator with very thin wires to reduce the heat leak. The Hall sensor itself has a resistance of about 1 Ω. When it is operated with the recommended current of 100 mA, it acts as a heater with power of 10 mW and it increases the temperature by up to 0.5 K. In this experiment we operate it with 10 mA and the temperature only changes by 0.1 K.

In future, when we need to monitor a lot of small grains of this crystal, the sensitivity of SQUID will be necessary.

3.5 Equipment Setup

In this section, I will illustrate how to assemble all the parts discussed in the previous sections together.

3.5.1 Inside the Cryogenic Refrigerator

In our experiment, we want to reach the temperature below 2 K for Mn12-acetate and below 1 K for Fe_8. To make sure we can reach the proper base temperature, the best option is to attach the sample holder directly to the 1K pot while we are testing Mn12-acetate, to the helium-3 pot for Fe_8. However, we also need a relatively high magnetic field. Both the 1K pot and the helium-3 pot are too far away from the center of the superconducting magnet and the maximum field can only reach around 1000 Gauss. To meet both cooling and magnetic field requirements, we add a stage made of OFHC with a thermal link to either the 1K pot or the helium-3 pot. It holds the sample holder close to the magnet. The setup is shown in Figure 3.19.

When heat is produced in either the Hall sensor or SMM crystals, the temperature on this extended stage will be higher than that on the 1K pot. The difference can be calculated by

$$\triangle T = \frac{PL}{\alpha A} \tag{3.3}$$

where P is the heat flow going through the thermal link, L is the lengh and A is the cross section area of thermal link, α is the thermal conductivity of the OFHC. When the Hall sensor continuously creates joule heat of 0.1 mW during the experiment, the temperature difference is

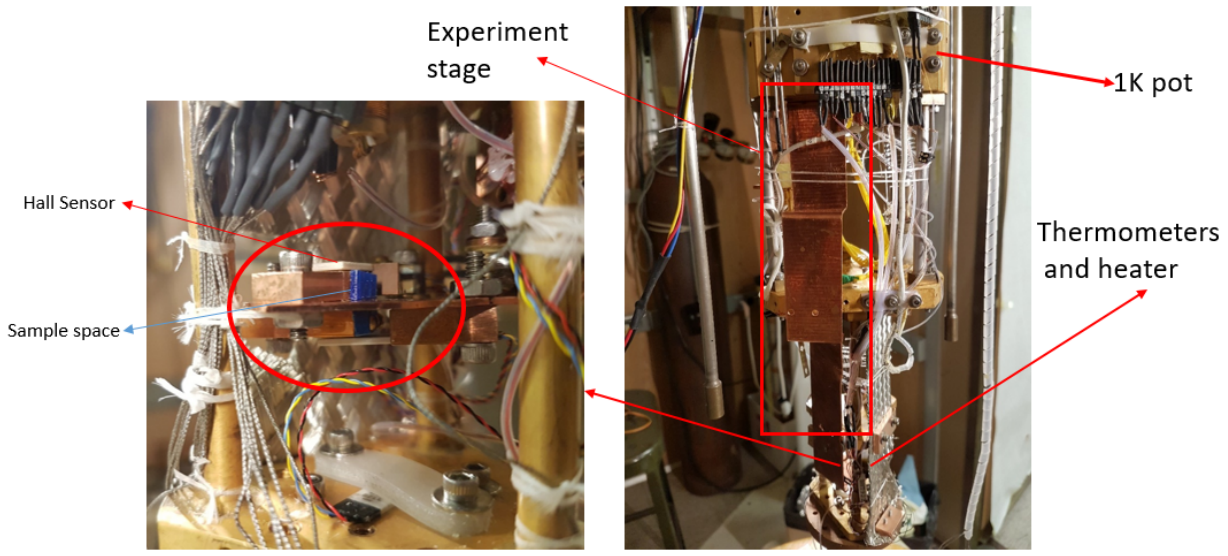

Figure 3.19: The Hall sensor and sample holder are set up inside the refrigerator.

about 10 to 20 mK. This is negligible for this experiment. After a magnetic avalanche, the heat flow and thus the temperature difference might be bigger, but we do not care about the temperature at that moment any more. The stage will cool down as we are resetting the system.

Two diode thermometers with standard curve were placed close to the sample holder. In case one of them failed to work during the experiment, we have another to use. These diode thermometers are good above 1.5 K. A germanium thermometer is placed on the helium-3 pot to monitor the temperature when we start to use Helium-3 circulation. None of these thermometers work properly when a strong magnetic field is applied. A Ruthenium oxide thermometer is added on the helium-3 stage in the last run, which works well in a strong magnetic field.

Two heaters are also installed on the stage, because we need to warm the crystals up above their blocking temperature occasionally.

A closer look at the Hall sensor and the sample holder can be seen in Figure 3.20. We have the copper sample holder with SMM crystals fixed on the extended stage. The cryogenic Hall sensor is also held on a OFHC bulk so the Joule heat from the Hall sensor can be transferred to the 1K pot quickly. The Hall sensor is carefully located in a position very close (about 1 mm above) to

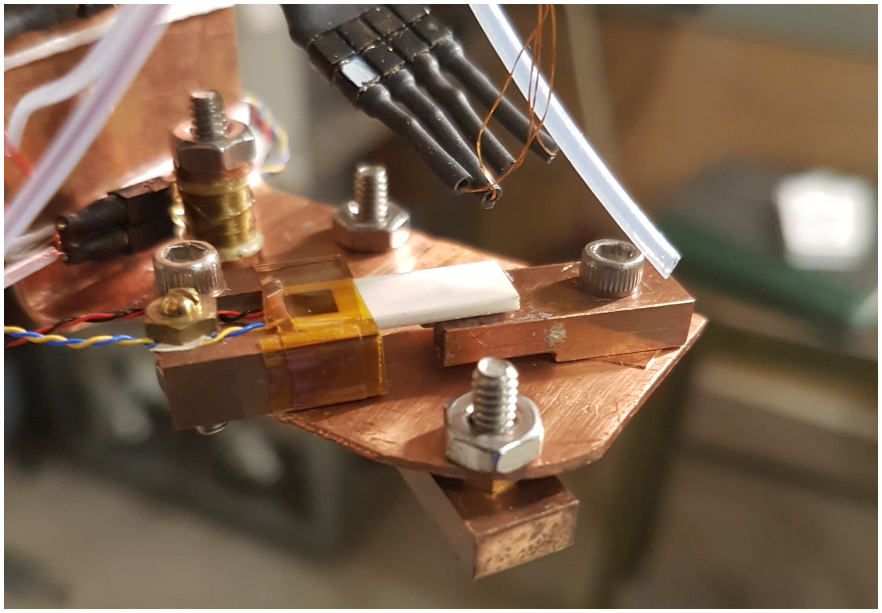

Figure 3.20: The Hall sensor and the sample holder

the crystals but not in touch with them. We want it to be close because we want the signals to be as big as possible. The magnetic field drops fast ($\sim r^{-3}$) with distance, so it is crucial to be close. At the same time, we do not want the Joule heat from the Hall sensor to flow to the crystals, so we leave a vacuum space between them as a thermal insulation.

After everything is set up inside the vacuum can, we tie all the floating wires with dental floss to somewhere away from the wall of the vacuum can. Because when we reach our base temperature, the vacuum can itself is still very "hot" at the helium-4 temperature (4.2K). Any touch between the equipment inside and the vacuum can will warm up our experiment stage.

3.5.2 Electronics Outside of the Cryogenic Refrigerator

To operate the experiment and read signals, we need to connect the equipment inside the refrigerator to the outside electronics. We have a junction box shown in Figure 3.21 to connect Hall sensors, heaters and various thermometers to the outside electronics.

Figure 3.22 shows the electronics for the Hall sensor. A DC power supply is used to supply a constant 10 mA current to the Hall sensor and an ammeter is used to monitor this current. A sensitive multimeter is used to read the Hall voltage.

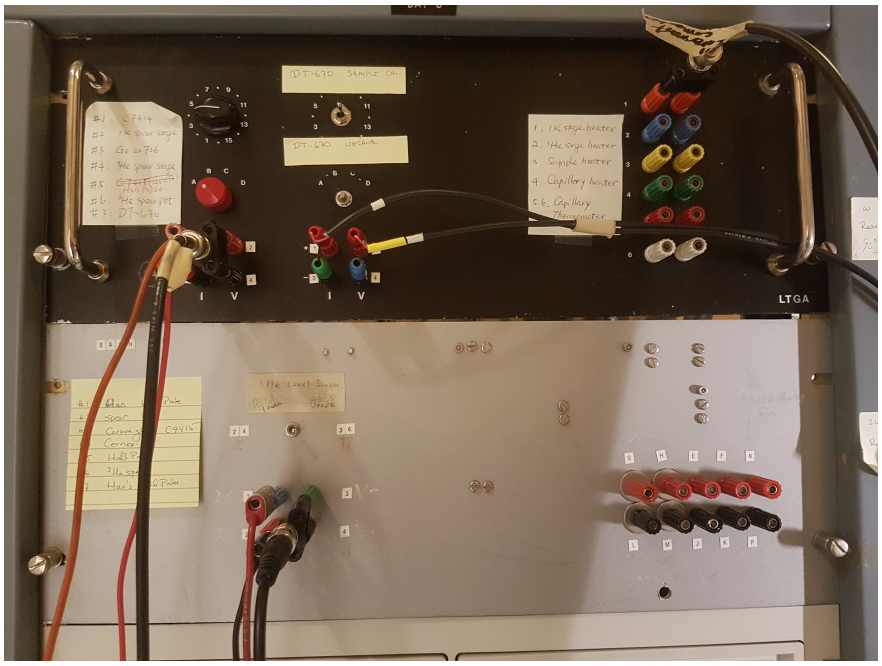

Figure 3.21: The junction box to connect the cold hardware inside the refrigerator and electronics outside.

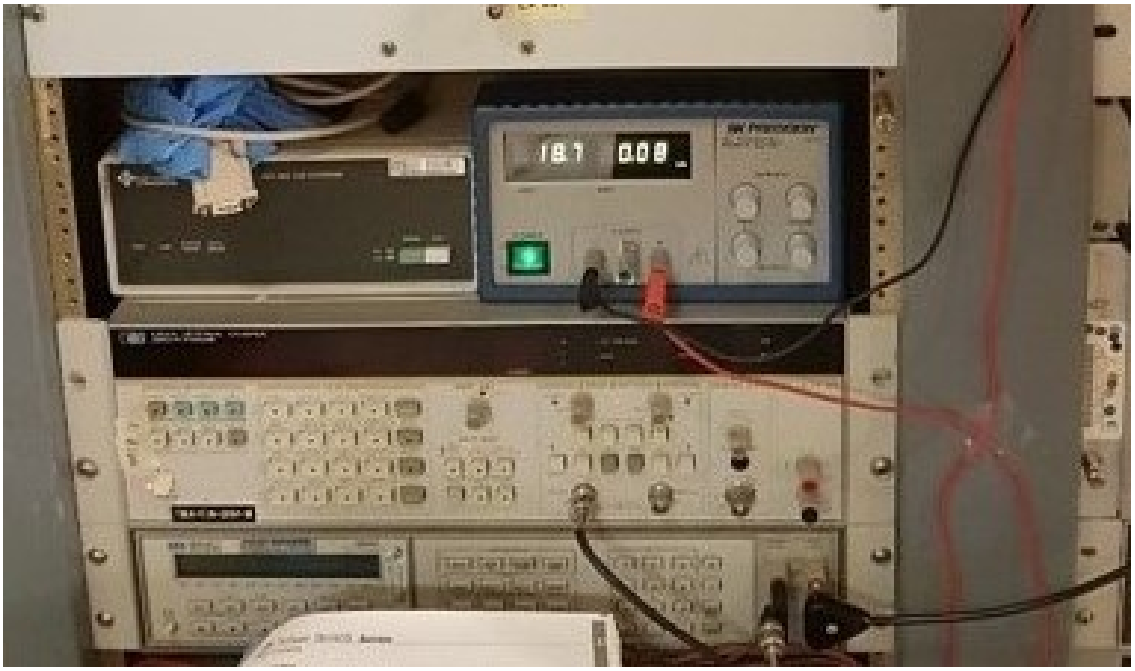

Figure 3.22: The power supply and multimeter connected to the Hall sensor

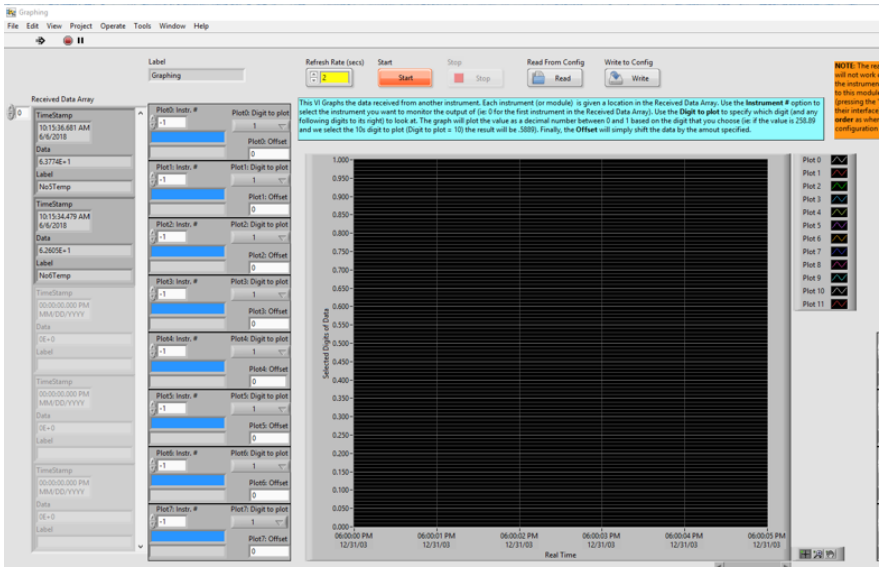

Figure 3.23: UI of the labview program

The superconducting magnet current controller has a readout port to show the value of its current. It is connected to a multimeter to be monitored and recorded. All the multimeters include a GPIB connection so they can communicate with a computer. A labview program is used to display and store all data, as shown in Figure 3.23.

With all the equipment set up correctly, we are ready to start the run.

4. EXPERIMENT RESULTS AND DATA ANALYSIS

This experiment includes four stages. First, the properties of Mn12-acetate crystals and the Hall sensor were tested. Second, after making sure the crystals can be magnetized properly and the Hall sensor can detect a magnetic avalanche, two gamma sources were placed outside of the refrigerator to check if avalanches can be triggered. In the third stage internal alpha source was introduced. Finally, some additional tests were done with Fe_8 crystals.

4.1 Pilot Run with the Mn12-Acetate

Before testing the Mn12-acetate crystals with radioactive sources, two things need to be confirmed. First, we want to make sure when the crystals are magnetized at a low temperature, that the magnetization can survive an external magnetic field whose direction is opposite to that of the magnetization. Second, we need to be confident that the crystals can experience a magnetic avalanche and the Hall sensor has enough sensitivity to detect it.

The first step was to see if the magnetization was stable under a reversed magnetic field. After successfully cooling down the fridge, a heater was turned on to warm up the crystals to a temperature above 3 K. Then the superconducting magnet was turned on to magnetize Mn12-acetate crystals. With the magnet on, the heater was turned off. Next we waited for 10 minutes to make sure the temperature dropped below 2 K. Finally, reverse the direction of the magnetic field and observe the reading of the Hall sensors.

The stability was tested at various temperatures. It showed the highest temperature at which the magnetization can survive the reversed magnetic field was 1.9 K, as shown in Figure 4.1 and Figure 4.2.

The next step was to show a magnetic avalanche. The ignition of an avalanche depends on the temperature and external magnetic field. To find the right conditions to trigger a magnetic avalanche, a reversed field was swept at a constant temperature (lower than 1.9 K). When the field reached a certain value, a magnetic avalanche was detected by the Hall sensor, as shown in Figure

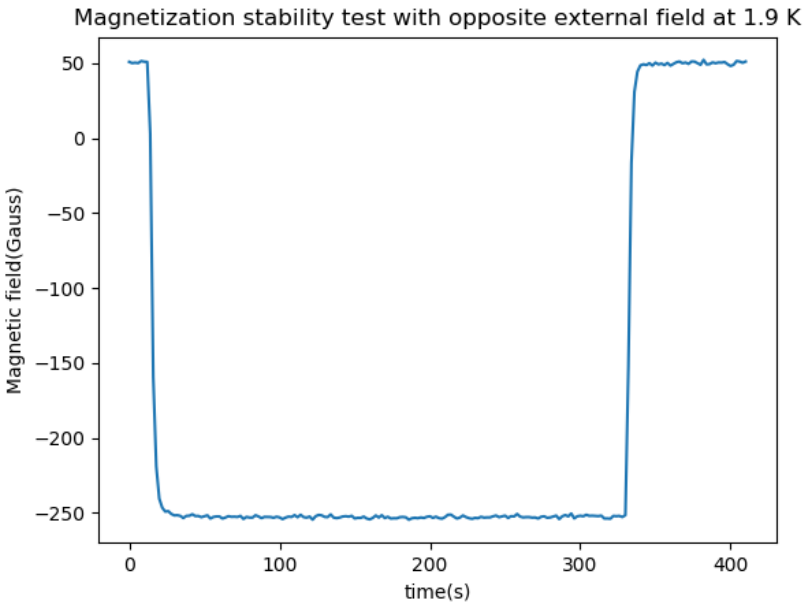

Figure 4.1: This shows how the magnetic field in the Hall sensor changed with time. The magnetized crystals were placed in a field in the opposite direction of the magnetization for 5 mins, the magnetization stayed the same after the external field was removed. This was done when the temperature was 1.9 K.

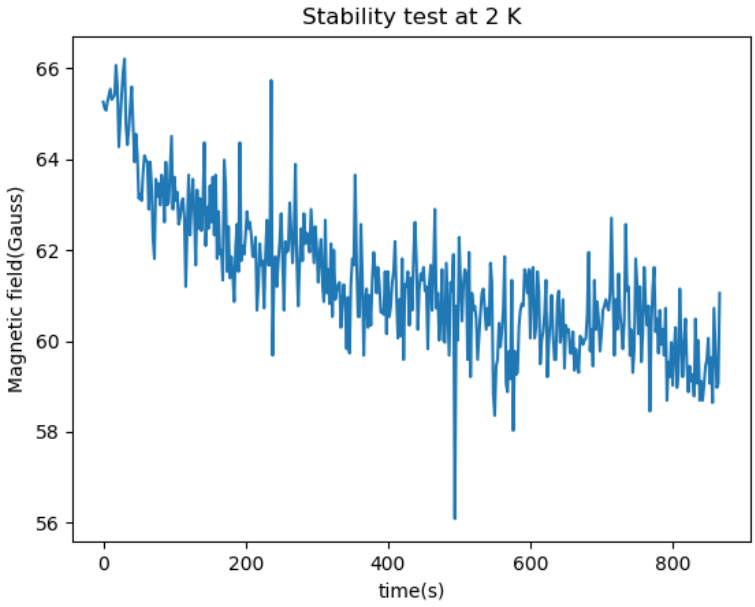

Figure 4.2: When the temperature was 2 K, the magnetized crystals slowly relaxed without an external field.

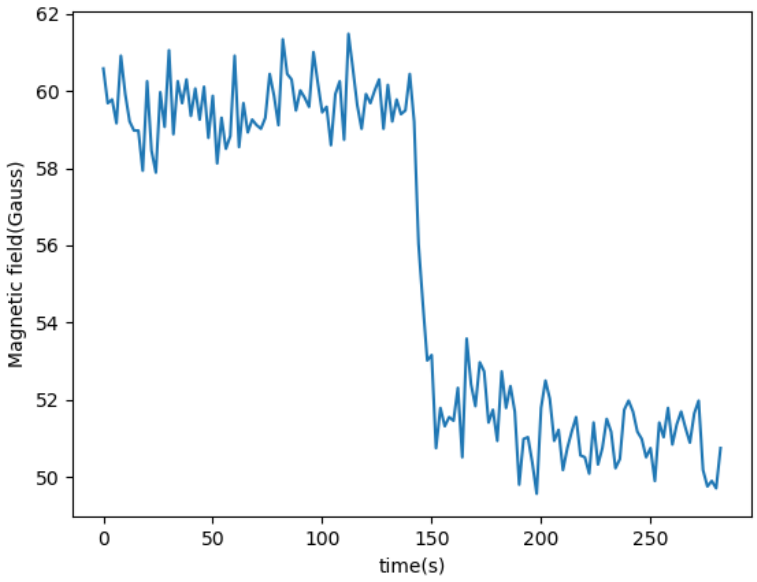

Figure 4.3: When the magnetized crystals were in a magnetic field in the opposite direction of the magnetization, a magnetic avalanche showed up and it was detected by the Hall sensor.

4.3.

The signal was about 10 gauss, smaller than the estimate from calculation of 100 gauss. It was reasonable though, since The distance between the active area of the Hall sensor was lager than the estimate. The actual distance was close to 2 mm instead of 1 mm in the estimate, which would reduce the signal in a factor of 1/8. Also, when it was estimated, we assumed that 100% of the molecules in the crystals were polarized in the same direction, which only happens in ideal condition. Another reason for the small signal is the alignment of the crystals, which is not exactly perpendicular to the active area of the Hall sensor, so the measured value is smaller than the actual field.

Both tests were repeated many times until it was sure the properties of the crystal were as expected and the Hall sensor was able to detect the signal.

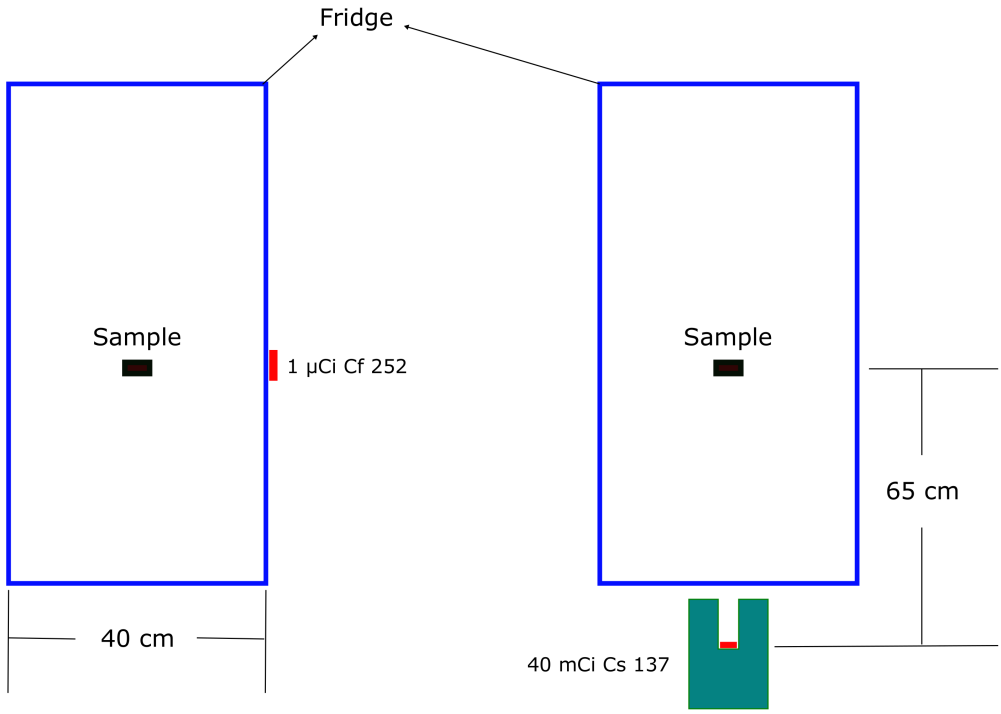

Figure 4.4: The setups to test Mn12-acetate crystals with external radioactive sources are shown here. In setup A on the left, a Cf-252 neutron source was attached on the outer wall of the refrigerator, it was 20 cm away from the crystals. In setup B on the right, a Cs-137 gamma source was placed below the refrigerator, it was 65 cm away from the crystals.

4.2 Experiments with External Sources

In the next few runs, we started to introduce various radioactive sources to test the main idea of this project: if a scattering of particles can trigger magnetic avalanches.

Initially, we placed the radioactive sources outside of the refrigerator, as shown in Figure 4.4. Two different kinds of sources were used in this test.

The first source tried was a californium-252 (Cf-252) neutron source with an activity of 1 μCi . The closest position to the crystals where it could be placed was on the outer wall of the dewar, which was 20 cm away from the Mn12-acetate crystals. We cannot see the exact location of the

Figure 4.5: **(a)** The laser was used to locate the crystals. **(b)** Location of the Cf-252 source.

sample holder after we close the dewar. To label the location, a low power laser beam in the horizontal direction was set up before closing the refrigerator, it pointed to the crystals. When we needed to use the Cf-252 source, it was placed at the bright spot left by the laser on the dewar wall. The high energy neutron source is harmful to the human body, so it was covered by several lead bricks during its use. The set-up is shown in Figure 4.5.

The face of the crystal space facing the source had a dimension of $3mm \times 3mm$. The Cf-252 source was manufactured on Oct. 01, 2017 and this experiment was operated on Aug. 03, 2018. With the half life of 2.6 years, a simple calculation showed neutrons will pass Mn12-acetate crystals at the rate of

$$activity \times 0.5^{\frac{t}{t_{1/2}}} \times \frac{3mm \times 3mm}{4\pi(2cm)^2} \times 3.7 \times 3.1\% = 0.06 \quad neutrons/second \tag{4.1}$$

The calculation includes that the spontaneous fission branching fraction which takes up 3.1%

of the total decay rate and an average of 3.7 neutrons are emitted per spontaneous fission. It did not include the attenuation by fridge walls. The average neutron energy is 2.13 MeV and the most probable energy is 0.70 MeV.

In this run, we managed to reach a temperature of 1.7 K. Without radioactive sources, the crystals were magnetized. An external reversed magnetic field was slowly swept from zero. The avalanches happened when the field reached around 2800 Gauss.

Two different tests were done with the 1 μCi Cf-252 neutron source. First, the crystals were magnetized and the reversed field of 2700 Gauss was applied. This is slightly below the value which will ignite a magnetic avalanche, analogous to the temperature of the superheated fluid in a bubble chamber being held slightly below its boiling temperature. The source was arranged at the position shown in Figure 4.5. The system was kept in this way for 30 minutes. During this period, there should be around 100 neutrons passing the sample space but no avalanche was detected. This was repeated twice and the same results were obtained.

A possible explanation for this result is that the external field must be closer to the critical point of 2800 Gauss, so another test was done. The magnetized crystals were placed in a reversed field again. Rather than holding the field constant, we slowly increased the field with time. Meanwhile, we were observing the magnetization of the crystals with the Cf-252 source 20 cm away. An avalanche was triggered around 2800 Gauss. In other words, the radioactive source did not appear to make any difference to the previous results without the source.

Both tests were also done with another radioactive source: a 4 mCi caesium-137 source. This source emits gamma rays with an energy of 0.6617 MeV. It has a much bigger activity comparing with the Cf-252 source used above, however, the result was the same. With or without this source, the behavior of the Mn12-acetate crystals was the same.

The null result from the Cs-137 source is as expected. Since the gamma rays from it can only make electron recoils which are very unlikely to trigger a magnetic avalanche as explained in Section 2.2.3.

This run showed that neither sources, at least in our setup, could trigger magnetic avalanches

in Mn12-acetate crystals. A possible explanation is that the neutron flux was too low, either due to the long distance between the source and the Mn12-acetate crystals or the attenuation of the refrigerator wall. Another possible reason is that the energy threshold of this specific material, Mn12-acetate, is higher than the radioactive source we used. Of course, it is also possible that the magnetic avalanches simply can not be triggered by a scattering of particles.

4.3 Experiments with an Internal Source

Although we did not see any avalanches triggered by the external sources in the last run, this does not necessarily mean that a scattering of particles is not able to ignite it. We redesigned the experiment to exclude the possible reasons mentioned in the last section. In the following run, we placed an americium-241 (Am-241) source inside the refrigerator. It was very close (about 2 mm) to the Mn12-acetate crystals and there was no material between them. The alpha particles from this source also had a higher energy than the neutrons from Cf-252.

Also, before this run, we carefully estimated the energy threshold of Mn12-acetate.

4.3.1 Energy Threshold

The most probable de Broglie wavelength of the neutrons from californium-252 is 34.2 fm, and the americium-241 emits alpha particles with a wavelength of 6.1 fm. Both are bigger than any nucleus in Mn12-acetate but much smaller than a Mn12-acetate molecule. As a result, the scattering will happen between the incoming particles and one single atomic nucleus.

There are several kinds of atoms in Mn12-acetate molecules: manganese, hydrogen, carbon, and oxygen. For the neutron source, hydrogen atoms have almost the same mass as neutrons, so they can absorb maximum recoil energy of $E_r = E_i$, where E_i is the kinetic energy of an incoming particle. So the Cf-252 will most probably deposit 0.7 MeV energy by a nuclear recoil. For the Am-241 source, carbon atoms has similar mass to the alpha particles, so they can absorb maximum recoil energy of $E_r = 0.36E_i$. The Am-241 source can provide alpha particles with kinetic energy of 5.486 MeV, so the maximum deposited energy is about 2 MeV, higher than that from the californium-252 source.

To trigger a magnetic avalanche, the maximum recoil energy E_r has to be above the energy threshold E_0 given by Equation 2.3. For Mn12-acetate, the spin of a single molecule is $J = 10$, the volume specific heat is $c_0 = 2 \times 10^{-9} eV \cdot K^{-1} \cdot nm^{-3}$, the potential barrier without external magnetic field is $U = 61K$, and the relaxation time prefactor is $\tau_0 = 2.1 \times 10^{-7} s$ [26]. We do not know the value of the thermal conductivity though, it could range from $10^{-7} m^2/s$ to $10^{-5} m^2/s$, corresponding to an energy threshold from 46 keV to 46.6 GeV. It is possible that the threshold falls between 0.7 MeV and 2 MeV, so alpha particles coming from the Am-241 can trigger a magnetic avalanche whereas neutrons from the Cf-252 can not.

4.3.2 Experimental Setup

As a result of the discussion above, we gave the Mn12-acetate crystals another try with a 1 μCi Am-241.

The Am-241 source was placed inside the fridge, about 2 mm away from the Mn12-acetate crystals, as shown in Figure 4.7. Even though it has similar activity to the Cf-252 source, the radioactive flux is much bigger due to the closer proximity.

Figure 4.7 also shows the experimental setup. Since alpha particles cannot penetrate even a thin layer of copper, the Am-241 source was placed next to one set of Mn12-acetate crystals. As mentioned in Section 3.3.4, the crystals were hermetically wrapped in silver epoxy to protect them, but alpha particles would be shielded by the epoxy in this way. To avoid this, the crystals close to the Am-241 source were only partially covered by the silver epoxy in this run, as shown in Figure 4.6. The epoxy was only used to keep the crystals in place.

In this setting, the crystals were exposed to alpha radioactive all the time during our experiment. It is impossible to remove the source to observe if it makes any difference during the experiment, therefor a control setup was placed nearby. The control setup also included about 10 crystals with similar dimension as those in the main setup, which sit in a sample holder and were bundled with a Hall sensor. The control setup was placed on the same stage as the main setup and was about 1 cm away, so both setups shared approximately the same magnetic field and temperature. Alpha particles can not penetrate the copper between two setups, so the control setup will not see the high

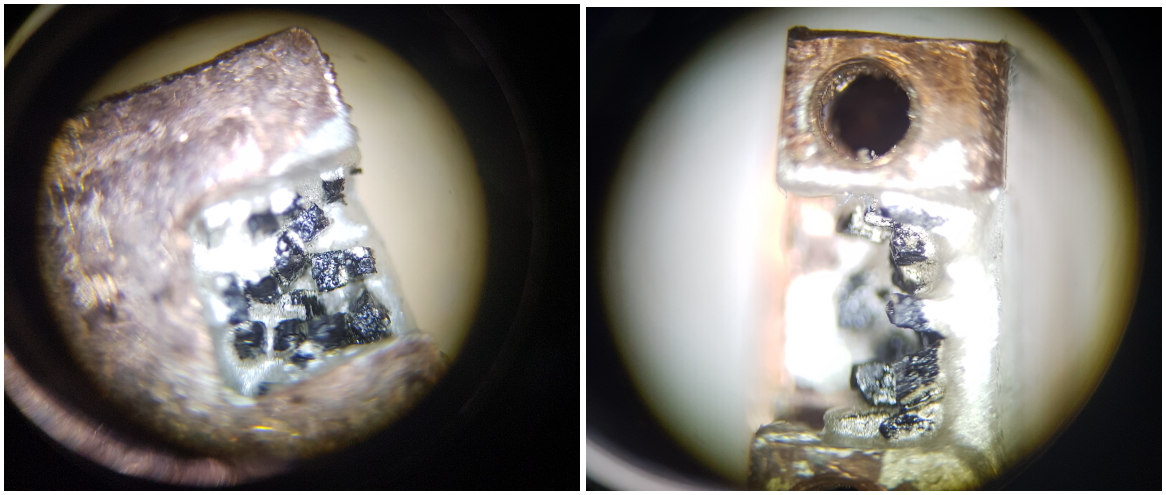

Figure 4.6: Mn12-acetate crystals partially covered by the silver epoxy.

energy particles whereas the main setup is exposed to them all the time.

Thermometers and heaters were placed on the same stage as before.

4.3.3 Operations and Results

After the refrigerator was cooled down to the base temperature of 1.7 K, the tests described in Section 4.1 were done again. The stability of the crystals in a reversed field was tested and confirmed, and we again observed that a swept magnetic field could trigger a magnetic avalanche. Thereafter, the behavior of Mn12-acetate crystals was observed under two different conditions: either in a swept magnetic field or in a constant one.

Similar to the last run, the crystals were magnetized at 3 K first, then cooled down to the base temperature so that the magnetization could be kept stable. A reversed field was applied and it was increased slowly from zero. When the reversed field reached a certain value, an avalanche was observed in the main setup, i.e., those Mn12-acetate crystals bundled with Am-241 source. At the same time, no avalanches was observed in the control setup, as shown in Figure 4.8.

This procedure was repeated several times. The results were the same every time except that the critical magnetic fields at which a magnetic avalanche was triggered were different, ranging from 4900 Gauss to 6000 Gauss. This variation is possibly due to a slight difference in temperature for

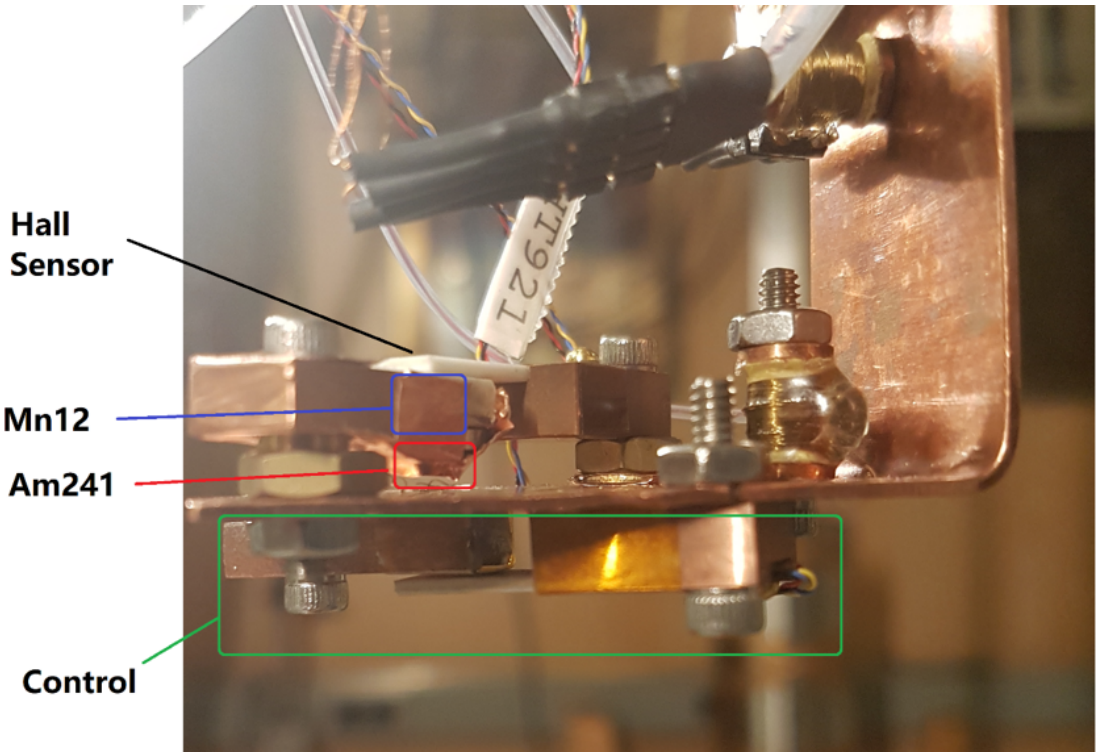

Figure 4.7: Two sets of Mn12-acetate crystals are placed in the refrigerator, one with Am-241 alpha source and the other one working as a control setup.

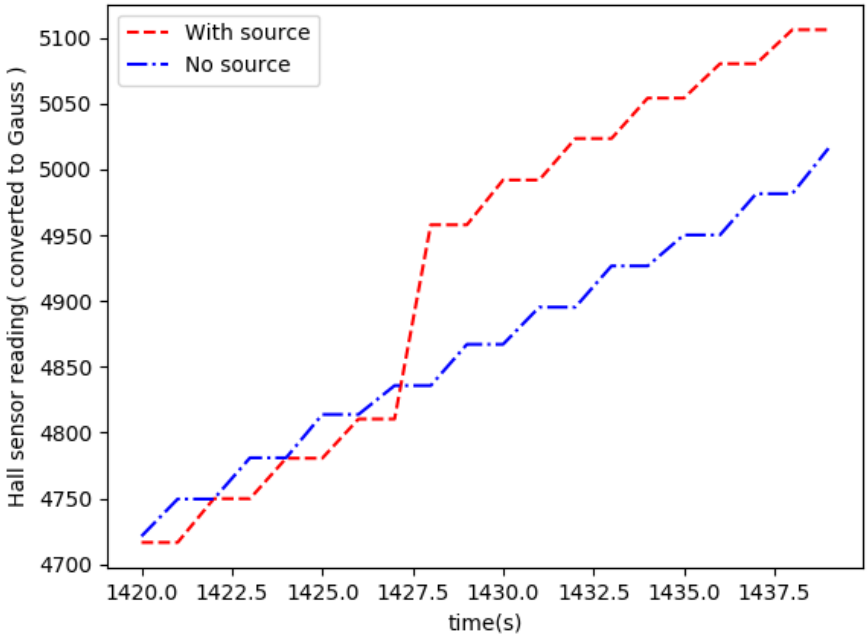

Figure 4.8: A magnetic avalanche was observed in the crystals with Am-241 source while none was observed in the control setup.

each test. Unfortunately, the thermometers we used in this run were carbon dioxide thermometers. Their resistances were strongly dependent on the magnetic field thus could not show the correct temperature when the field was swept.

This suggested that magnetic avalanches could be triggered by scattering of particles when the external field was swept. However, this is not enough for it to be a practical particle detector. According to Equation 2.3, the energy threshold decreases when the reversed magnetic field increase, as long as the field is not big enough to eliminate the barrier between the double wells, in which case magnetic avalanches are impossible. If a magnetic avalanche can only be triggered by the scattering of particles when the field was swept, there is only a small fraction of operation time when the field is big so that we have a low threshold. As a particle detector, especially when it is used to search rare dark matter events, the live time is important, so it will be much better if similar results could be shown for a constant magnetic field. This is what was tested in the next step.

The Mn12-acetate crystals were magnetized first, then a reversed field was applied. The field was kept constant for about 10 minutes. If no avalanche showed up, we increased the reversed field a little bit and waited for another 10 minutes. This was repeated until the field was about 6500 Gauss when an avalanche was observed in the crystals close to the Am-241 source. Meanwhile, nothing was observed in the control setup, as shown in Figure 4.9. This result implies that an avalanche can be ignited in a constant field.

To confirm the signals observed were actually magnetic avalanches as expected, two things were done. First, each time after an avalanche was observed, the external magnetic field was removed and a heater was turned on to demagnetize the crystals. It was clear that the magnetization of the main setup and control setup pointed in opposite directions after the avalanche, as shown in Figure 4.10. Note that initially, the magnetization directions of both crystal sets were the same since they were magnetized by the same external field. This implied that the magnetization of those crystals close to the Am-241 source was flipped to the other direction, while it is unchanged in the control setup.

It is also worth to mention that the electronics of both setups were connected to the same power

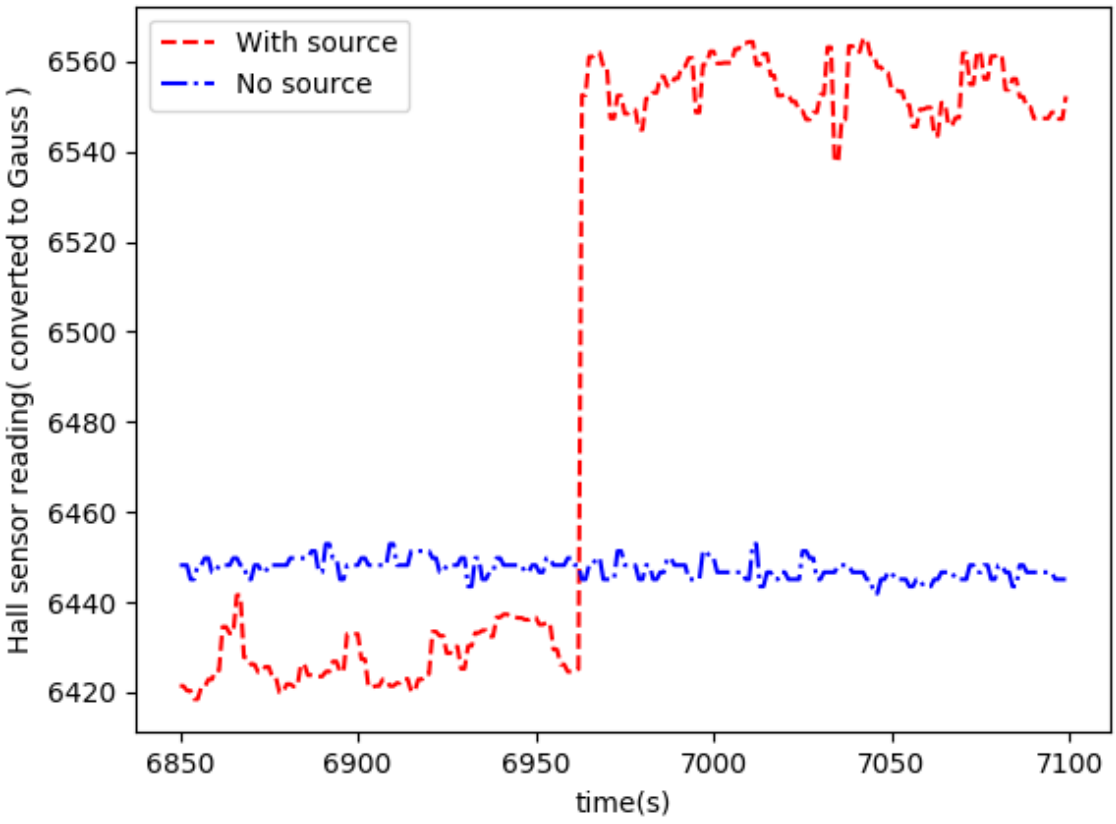

Figure 4.9: The magnetized Mn12-acetate crystals are placed in a constant reversed field. After several minutes, crystals close to the source experienced a magnetic avalanche whereas nothing happened to the control setup.

outlet. If the avalanche signals were false, due to electronic noise, it should appear in both setups. So it is safe to say that our signals were not from an electronics glitch.

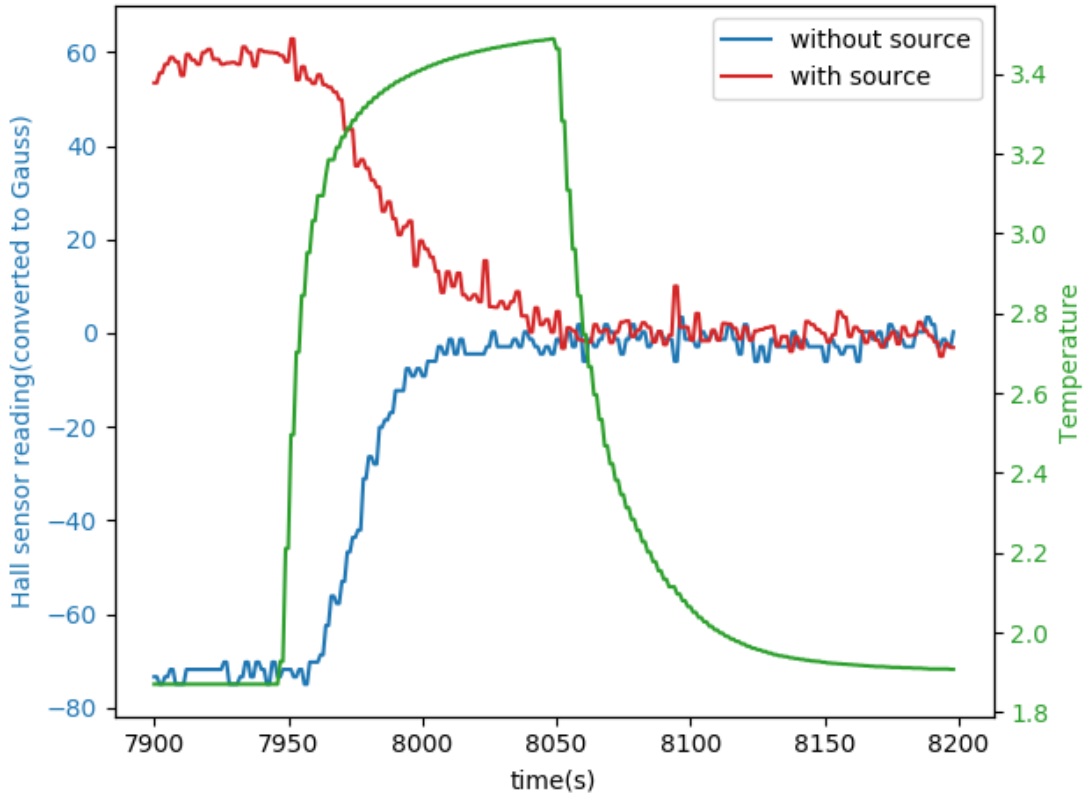

Figure 4.10: Demagnetization of Mn12 crystals after an avalanche was observed. The blue line showed the magnetic field close to the crystals in the control setup, the red line showed that in the main setup. The green line showed the change in temperature. The heater was turned on when t = 7950 s, and was turned off when t = 8050. This showed that the magnetization of crystals in two setups pointed to the opposite direction after an avalanche.

Secondly, since a resonant quantum tunneling can also relax the magnetization of an Mn12-acetate crystal, to make sure what was observed in this work is actually a magnetic avalanche, we compared our data with resonant quantum tunneling in literature [27]. The magnetization jump in our experiment took less than one second, while quantum tunneling takes around 1 minute (at these temperatures) to only partially demagnetize the crystal, as shown in the Figure 4.11.

In short, at the same temperature and the same external magnetic field, the Mn12-acetate crystals close to the Am-241 source showed magnetic avalanches while the control setup far from the source did not show anything, which suggested that the avalanches were triggered by high energy alpha particles. This shows that avalanches can be ignited by particle interactions.

4.4 Fe_8 Crystals

Initially, the refrigerator we used could only go down to 1.7 Kelvin, due to impurities in the Helium-3 tank. After some cleaning and adjustments, we could cool down to 0.5 K. At this temperature, we can test a large variety of SMM crystals. Some preliminary tests have been done with Fe_8 crystals described in this section.

4.4.1 Crystal Preparation

It is not possible to identify the easy axis from the shape of Fe_8 crystals. Therefor, they were sitting in the sample holder at random orientations. A dozen of single crystals were placed close to the Hall sensor. In the future, we will index the crystal structure with X-ray Powder Diffraction (XRD), which will hopefully allow for uniform crystal orientation.

Fe_8 crystals are vulnerable in air or vacuum, so they were also protected by silver epoxy, as shown in Figure 4.12. Similar to the experiments we had done with the Mn12-acetate crystals, the Fe_8 crystals were positioned close to the active area of the Hall sensor with the vacuum between them acting as thermal insulation.

4.4.2 Stability Test

Some tests were done to make sure that the Fe_8 crystals could be properly magnetized in our refrigerator and that the Hall sensor had enough sensitivity to read the magnetization.

A heater was turned on to warm up the crystals to about 2 K. A magnetic field of 1 T was applied afterward. The next step was turning off the heater and waiting for the temperature to drop back to the lowest temperature we can reach (around 0.5 K with Helium-3 circulation). The crystals should be magnetized at that moment. The magnetic field was then removed.

At that moment, the reading of the Hall sensor was about 40 Gauss without the external mag-

netic field. To make sure this was not a measurement error (due to the zero point of the Hall sensor shifting in the strong magnetic field), the crystals were warmed up again and the change in Hall sensor voltage is shown in Figure 4.13. While the temperature rose up, the magnetization was relaxed. This confirmed that the crystals were magnetized before warming up. Note that the germanium thermometer giving the temperature data in this figure was placed on the helium-3 stage, not the stage holding the Fe_8 crystals, so the temperature recorded was higher than the actual temperature of the crystals. Another RuO_2 thermometer close to the crystals showed the relaxation started when the temperature reached about 1 K. The data from the RuO_2 thermometer was unfortunately not recorded.

Next we performed the stability test. The magnetized crystals are placed in the external field whose direction is anti-parallel to the magnetization. The result is shown in Figure 4.14. The magnetization is stable under a reversed field up to about 1200 Gauss.

4.4.3 Search for Magnetic Avalanches in Fe_8

After we were confident we could magnetize the crystals and that the magnetization would remain stable, efforts were made to search for magnetic avalanches.

Similar to what had been done with the Mn12-acetate crystals, Fe_8 crystals were magnetized and an external field with direction anti-parallel to the magnetization was then applied. The external field was slowly increased from zero to 1 T. There was only once when two abrupt changes in the Hall sensor reading were observed, as shown in Figure 4.15. We were not able to see similar jumps when the procedure was repeated. Therefor it is possible it was just an electronic glitch.

An external gamma source (Cs-137) was placed close to the refrigerator thereafter. No avalanche was observed in this configuration as well. This was comforting to some point, because it did not contradict our assumption that the magnetic bubble chamber is capable of rejecting electron recoils.

More research will be done with the Fe_8 crystals. It is possible that they need a lower temperature environment to experience a magnetic avalanche. In that case, we will further tweak the refrigerator or move to another cryostat.

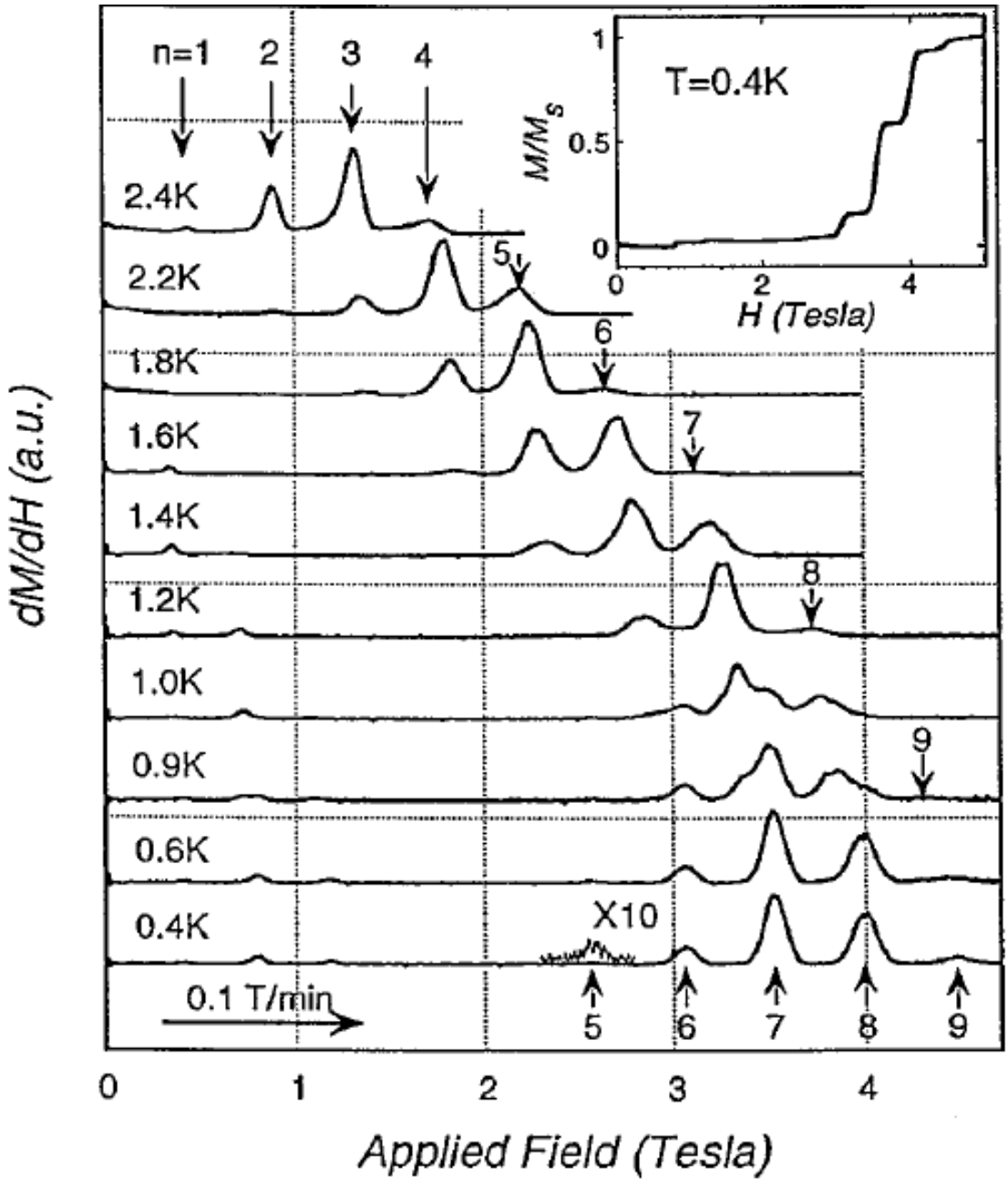

Figure 4.11: Magnetic hysteresis of a small Mn12 single crystal at different temperatures when magnetic field scanning speed is 0.1 T/min. The peaks in this graph are due to resonant quantum tunneling which relaxed the magnetization much slower than magnetic avalanches (see Figure 4.9). The dimension of the crystals used here was $50 \times 50 \times 300 \mu m^3$. Reprinted with permission from [27].

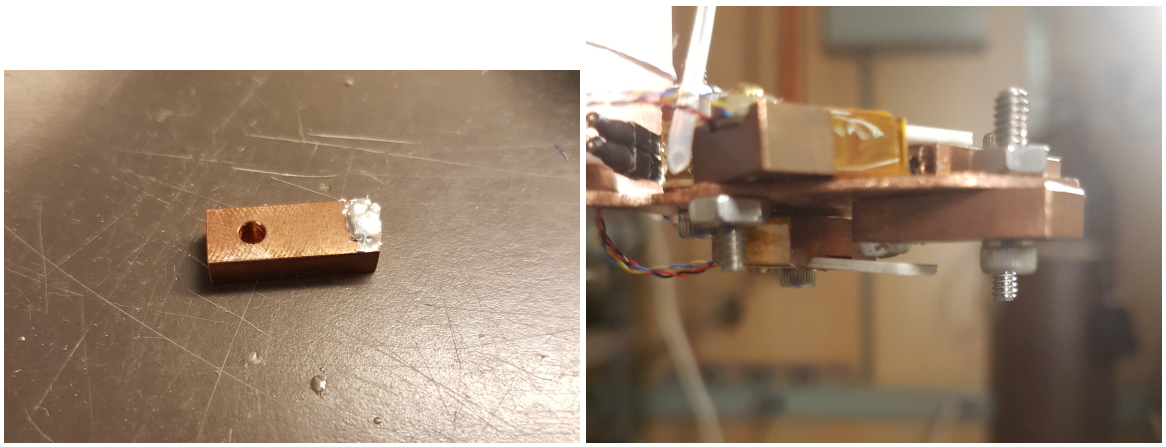

Figure 4.12: The sample holder for the Fe_8 crystals (left) and its position in the refrigerator (right).

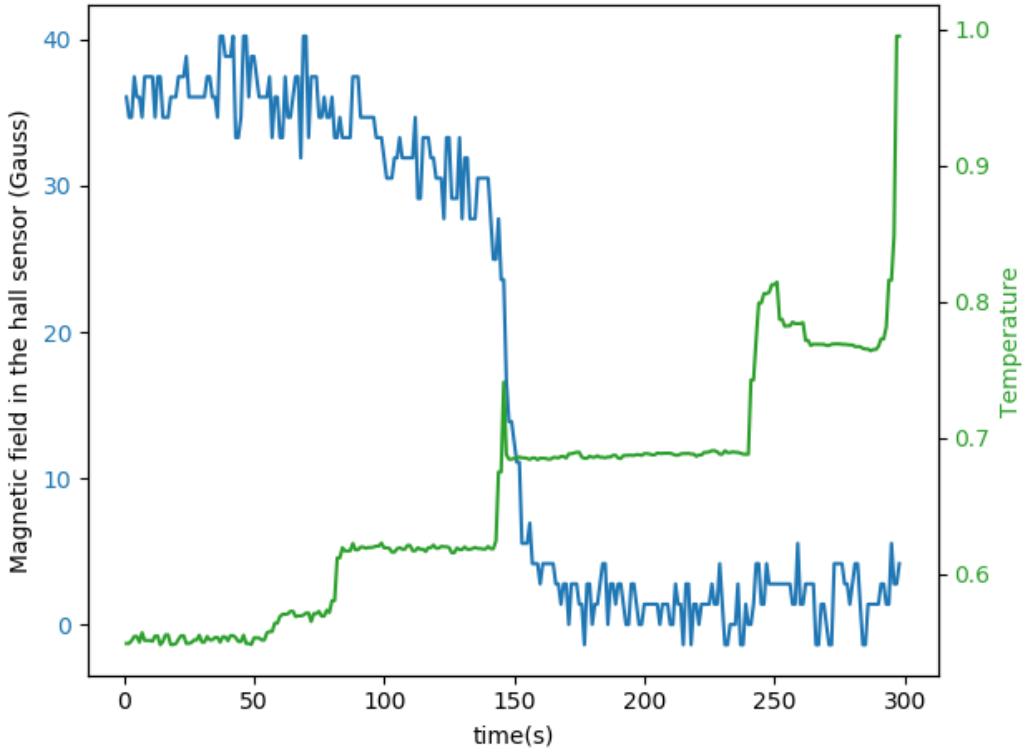

Figure 4.13: When the $Fe8$ crystals were warmed up, the reading from the Hall sensor jumped back to zero, this showed the crystals were magnetized before the heater was turned on.

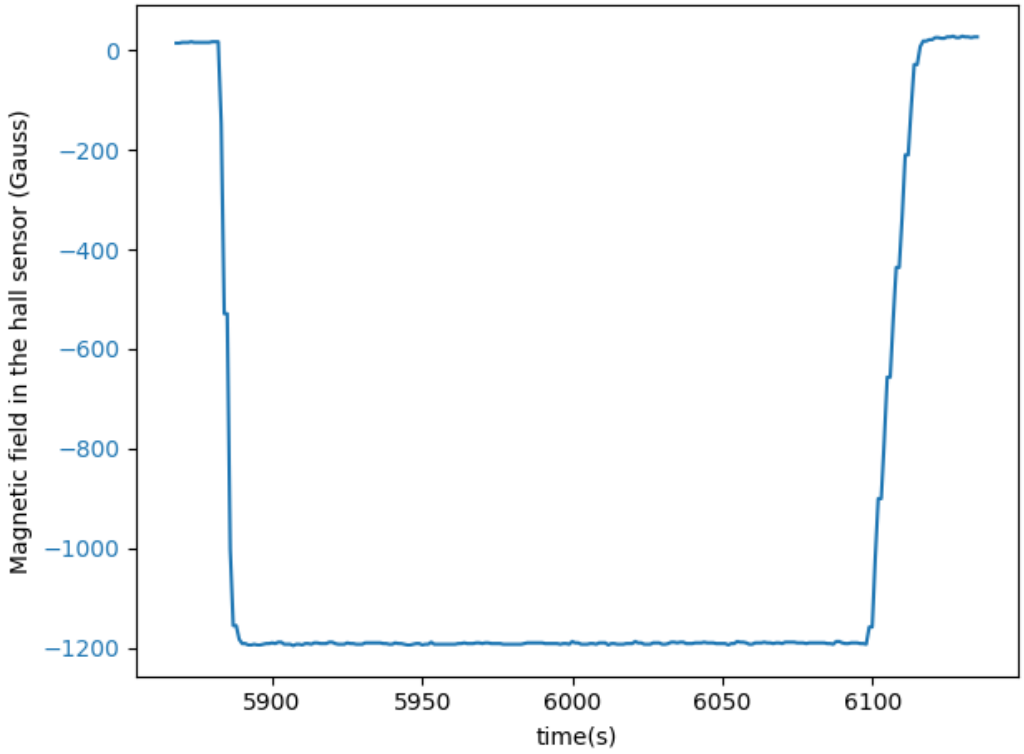

Figure 4.14: The Fe_8 crystals were initially magnetized, as shown in the none zero reading of the Hall sensor, they were then placed in a reversed field for about 4 mins. After the field was removed, the magnetization did not change.

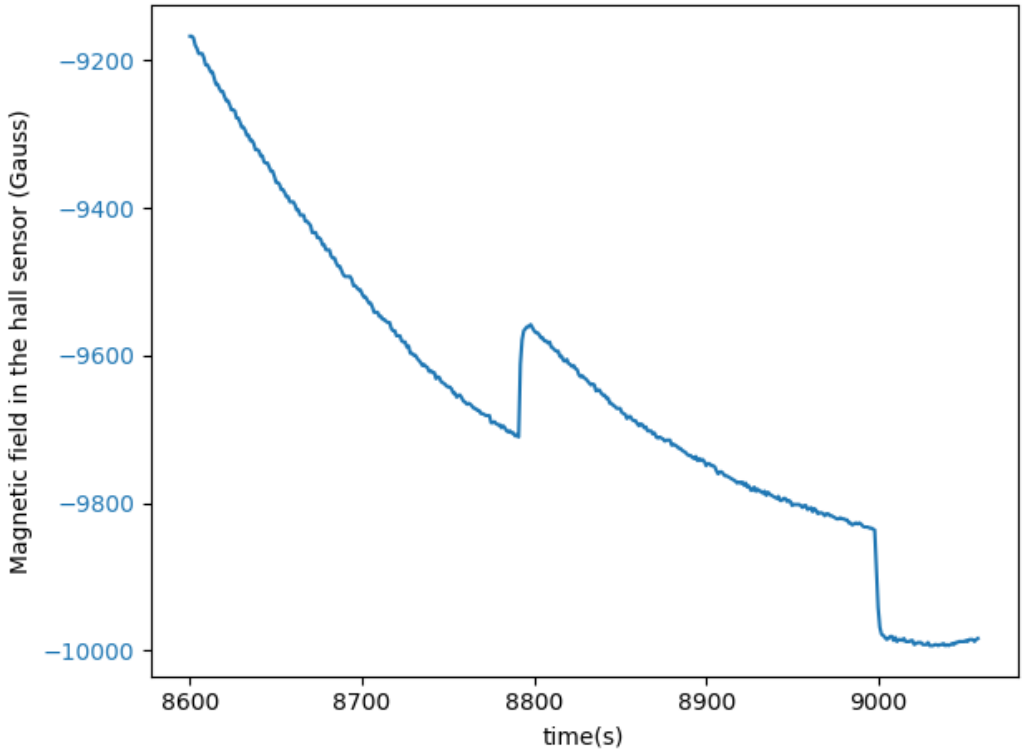

Figure 4.15: Two jumps during scanning the field. If they are magnetic avalanches, the left one was in the wrong direction, while the second one was in the right direction.

5. SUMMARY AND FUTURE PLANS

5.1 Summary of the Work

A low threshold detector will benefit the search for dark matter. The idea of the magnetic bubble chamber provided a new way to achieve a lower threshold with natural electron recoil rejection, but it was a question if it can work experimentally. The work in this dissertation tried to answer the question that if a scattering of particles can trigger a magnetic avalanche in an SMM crystal.

We used two sets of Mn12-acetate crystals. One set was bundled with an Am-241 alpha source, the other one was not close to the source which worked as a control setup. Our experiment showed magnetic avalanches were triggered in the main setup but not in the control setup. This suggested that avalanches were triggered by high energy alpha particles.

The energy threshold of Mn12-acetate we used is quite high as shown in both the calculation and the experiment. However, once we know the concept is working, it opens the door to test many other kinds of SMM materials currently existing and those can be newly synthesized to better suit the need to detect dark matter. Considering that the parameters from different SMM varies widely, it has the potential to reach a low threshold.

5.2 Future Plans

This work made a prototype of the magnetic bubble chamber. A lot more needs to be done in the future in order that it can function as a practical detector.

1. A lot of other kinds of SMM materials are available to test, some of them might lead to better results. Currently, our refrigerator can reach a base temperature of as low as 480 mK. With some modifications, there is a good chance that we can lower it down to 350 mK. This should be sufficient to test most SMM materials.

2. It will be very helpful to have a systematic approach to quantify some properties of various SMM materials. The value of the thermal conductivity is crucial to estimate the energy

threshold, but it is not known for most SMM materials. In the majority of cases, the synthesized SMM crystals are very small (in the order of mm), so it is not easy to do the measurement. The relaxation time and the heat capacity of the crystals also need to be measured. These quantities will help to choose some promising candidates among hundreds of SMM materials to test.

3. A cryostat that cools down to a lower temperature and stays very stable is preferred. Our refrigerator can keep the temperature as low as 0.5 Kelvin, but it is not very stable. Some SMM materials require a lower temperature to exhibit magnetic avalanches. One way is to place SMM crystals in the helium-3 liquid in the helium-3 pot which can provide a stable temperature environment. A dilution refrigerator is also an option.

4. The Hall sensor can be replaced by another magnetometer (SQUID, for example). This can benefit the experiment in two ways: On one hand, the sensitivity of the SQUID is much better. For some kinds of SMMs, only very tiny crystals can be synthesized, the signals from a magnetic avalanche are thus small. A highly sensitive magnetometer is essential in this case. On the other hand, the Joule heat from the hall sensor keeps the experiment stage from reaching a lower temperature. The SQUID does not have this problem.

REFERENCES

[1] J. H. Oort, "The force exerted by the stellar system in the direction perpendicular to the galactic plane and some related problems," *Bulletin of the Astronomical Institutes of the Netherlands*, vol. 6, p. 249, Aug 1932.

[2] F. Zwicky, "Republication of: The redshift of extragalactic nebulae," *General Relativity and Gravitation*, vol. 41, pp. 207–224, Jan 2009.

[3] V. C. Rubin, "Dark matter in spiral galaxies," *Scientific American*, vol. 248, no. 6, pp. 96–109, 1983.

[4] M. Milgrom, "A Modification of the Newtonian dynamics as a possible alternative to the hidden mass hypothesis," *Astrophys. J.*, vol. 270, pp. 365–370, 1983.

[5] D. Clowe, M. Bradač, A. H. Gonzalez, M. Markevitch, S. W. Randall, C. Jones, and D. Zaritsky, "A direct empirical proof of the existence of dark matter," *The Astrophysical Journal*, vol. 648, pp. L109–L113, Aug 2006.

[6] C. Alcock, R. A. Allsman, D. R. Alves, T. S. Axelrod, A. C. Becker, D. P. Bennett, K. H. Cook, N. Dalal, A. J. Drake, K. C. Freeman, M. Geha, K. Griest, M. J. Lehner, S. L. Marshall, D. Minniti, C. A. Nelson, B. A. Peterson, P. Popowski, M. R. Pratt, P. J. Quinn, C. W. Stubbs, W. Sutherland, A. B. Tomaney, T. Vandehei, and D. Welch, "The MACHO project: Microlensing results from 5.7 years of large magellanic cloud observations," *The Astrophysical Journal*, vol. 542, pp. 281–307, Oct 2000.

[7] Tisserand, P., Le Guillou, L., Afonso, C., Albert, J. N., Andersen, J., Ansari, R., Aubourg, É., Bareyre, P., Beaulieu, J. P., Charlot, X., Coutures, C., Ferlet, R., Fouqué, P., Glicenstein, J. F., Goldman, B., Gould, A., Graff, D., Gros, M., Haissinski, J., Hamadache, C., de Kat, J., Lasserre, T., Lesquoy, É., Loup, C., Magneville, C., Marquette, J. B., Maurice, É., Maury, A., Milsztajn, A., Moniez, M., Palanque-Delabrouille, N., Perdereau, O., Rahal, Y. R., Rich, J., Spiro, M., Vidal-Madjar, A., Vigroux, L., and S. Zylberajch (The EROS-2 collaboration),

"Limits on the macho content of the galactic halo from the eros-2 survey of the magellanic clouds," *A&A*, vol. 469, no. 2, pp. 387–404, 2007.

[8] L. S. Kisslinger and D. Das, "A brief review of dark matter," *International Journal of Modern Physics A*, vol. 34, no. 27, p. 1930013, 2019.

[9] M. Battaglieri *et al.*, "US Cosmic Visions: New Ideas in Dark Matter 2017: Community Report," in *U.S. Cosmic Visions: New Ideas in Dark Matter College Park, MD, USA, March 23-25, 2017*, 2017.

[10] M. Schumann, "Direct detection of WIMP dark matter: concepts and status," *Journal of Physics G: Nuclear and Particle Physics*, vol. 46, p. 103003, Aug 2019.

[11] R. Agnese, A. J. Anderson, T. Aralis, T. Aramaki, I. J. Arnquist, W. Baker, D. Balakishiyeva, D. Barker, R. Basu Thakur, D. A. Bauer, T. Binder, M. A. Bowles, P. L. Brink, R. Bunker, B. Cabrera, D. O. Caldwell, R. Calkins, C. Cartaro, D. G. Cerdeño, Y. Chang, H. Chagani, Y. Chen, J. Cooley, B. Cornell, P. Cushman, M. Daal, P. C. F. Di Stefano, T. Doughty, L. Esteban, E. Fascione, E. Figueroa-Feliciano, M. Fritts, G. Gerbier, M. Ghaith, G. L. Godfrey, S. R. Golwala, J. Hall, H. R. Harris, Z. Hong, E. W. Hoppe, L. Hsu, M. E. Huber, V. Iyer, D. Jardin, A. Jastram, C. Jena, M. H. Kelsey, A. Kennedy, A. Kubik, N. A. Kurinsky, A. Leder, B. Loer, E. Lopez Asamar, P. Lukens, D. MacDonell, R. Mahapatra, V. Mandic, N. Mast, E. H. Miller, N. Mirabolfathi, R. A. Moffatt, B. Mohanty, J. D. Morales Mendoza, J. Nelson, J. L. Orrell, S. M. Oser, K. Page, W. A. Page, R. Partridge, M. Pepin, M. Peñalver Martinez, A. Phipps, S. Poudel, M. Pyle, H. Qiu, W. Rau, P. Redl, A. Reisetter, T. Reynolds, A. Roberts, A. E. Robinson, H. E. Rogers, T. Saab, B. Sadoulet, J. Sander, K. Schneck, R. W. Schnee, S. Scorza, K. Senapati, B. Serfass, D. Speller, M. Stein, J. Street, H. A. Tanaka, D. Toback, R. Underwood, A. N. Villano, B. von Krosigk, B. Welliver, J. S. Wilson, M. J. Wilson, D. H. Wright, S. Yellin, J. J. Yen, B. A. Young, X. Zhang, and X. Zhao, "Low-mass dark matter search with cdmslite," *Phys. Rev. D*, vol. 97, p. 022002, Jan 2018.

[12] D. S. Akerib, J. Alvaro-Dean, M. S. Armel-Funkhouser, M. J. Attisha, L. Baudis, D. A.

Bauer, J. Beaty, P. L. Brink, R. Bunker, S. P. Burke, B. Cabrera, D. O. Caldwell, D. Callahan, J. P. Castle, C. L. Chang, R. Choate, M. B. Crisler, P. Cushman, R. Dixon, M. R. Dragowsky, D. D. Driscoll, L. Duong, J. Emes, R. Ferril, J. Filippini, R. J. Gaitskell, M. Haldeman, D. Hale, D. Holmgren, M. E. Huber, B. Johnson, W. Johnson, S. Kamat, M. Kozlovsky, L. Kula, S. Kyre, B. Lambin, A. Lu, R. Mahapatra, A. G. Manalaysay, V. Mandic, J. May, R. McDonald, B. Merkel, P. Meunier, N. Mirabolfathi, S. Morrison, H. Nelson, R. Nelson, L. Novak, R. W. Ogburn, S. Orr, T. A. Perera, M. C. Perillo Isaac, E. Ramberg, W. Rau, A. Reisetter, R. R. Ross, T. Saab, B. Sadoulet, J. Sander, C. Savage, R. L. Schmitt, R. W. Schnee, D. N. Seitz, B. Serfass, A. Smith, G. Smith, A. L. Spadafora, K. Sundqvist, J.-P. F. Thompson, A. Tomada, G. Wang, J. Williams, S. Yellin, and B. A. Young, "First results from the cryogenic dark matter search in the soudan underground laboratory," *Phys. Rev. Lett.*, vol. 93, p. 211301, Nov 2004.

[13] R. Agnese, A. J. Anderson, M. Asai, D. Balakishiyeva, R. Basu Thakur, D. A. Bauer, J. Beaty, J. Billard, A. Borgland, M. A. Bowles, D. Brandt, P. L. Brink, R. Bunker, B. Cabrera, D. O. Caldwell, D. G. Cerdeno, H. Chagani, Y. Chen, M. Cherry, J. Cooley, B. Cornell, C. H. Crewdson, P. Cushman, M. Daal, D. DeVaney, P. C. F. Di Stefano, E. D. C. E. Silva, T. Doughty, L. Esteban, S. Fallows, E. Figueroa-Feliciano, G. L. Godfrey, S. R. Golwala, J. Hall, S. Hansen, H. R. Harris, S. A. Hertel, B. A. Hines, T. Hofer, D. Holmgren, L. Hsu, M. E. Huber, A. Jastram, O. Kamaev, B. Kara, M. H. Kelsey, S. Kenany, A. Kennedy, M. Kiveni, K. Koch, A. Leder, B. Loer, E. Lopez Asamar, R. Mahapatra, V. Mandic, C. Martinez, K. A. McCarthy, N. Mirabolfathi, R. A. Moffatt, R. H. Nelson, L. Novak, K. Page, R. Partridge, M. Pepin, A. Phipps, M. Platt, K. Prasad, M. Pyle, H. Qiu, W. Rau, P. Redl, A. Reisetter, R. W. Resch, Y. Ricci, M. Ruschman, T. Saab, B. Sadoulet, J. Sander, R. L. Schmitt, K. Schneck, R. W. Schnee, S. Scorza, D. N. Seitz, B. Serfass, B. Shank, D. Speller, A. Tomada, S. Upadhyayula, A. N. Villano, B. Welliver, D. H. Wright, S. Yellin, J. J. Yen, B. A. Young, and J. Zhang, "Search for low-mass weakly interacting massive particles with supercdms," *Phys. Rev. Lett.*, vol. 112, p. 241302, Jun 2014.

[14] D. S. Akerib, H. M. Araújo, X. Bai, A. J. Bailey, J. Balajthy, S. Bedikian, E. Bernard, A. Bernstein, A. Bolozdynya, A. Bradley, D. Byram, S. B. Cahn, M. C. Carmona-Benitez, C. Chan, J. J. Chapman, A. A. Chiller, C. Chiller, K. Clark, T. Coffey, A. Currie, A. Curioni, S. Dazeley, L. de Viveiros, A. Dobi, J. Dobson, E. M. Dragowsky, E. Druszkiewicz, B. Edwards, C. H. Faham, S. Fiorucci, C. Flores, R. J. Gaitskell, V. M. Gehman, C. Ghag, K. R. Gibson, M. G. D. Gilchriese, C. Hall, M. Hanhardt, S. A. Hertel, M. Horn, D. Q. Huang, M. Ihm, R. G. Jacobsen, L. Kastens, K. Kazkaz, R. Knoche, S. Kyre, R. Lander, N. A. Larsen, C. Lee, D. S. Leonard, K. T. Lesko, A. Lindote, M. I. Lopes, A. Lyashenko, D. C. Malling, R. Mannino, D. N. McKinsey, D.-M. Mei, J. Mock, M. Moongweluwan, J. Morad, M. Morii, A. S. J. Murphy, C. Nehrkorn, H. Nelson, F. Neves, J. A. Nikkel, R. A. Ott, M. Pangilinan, P. D. Parker, E. K. Pease, K. Pech, P. Phelps, L. Reichhart, T. Shutt, C. Silva, W. Skulski, C. J. Sofka, V. N. Solovov, P. Sorensen, T. Stiegler, K. O'Sullivan, T. J. Sumner, R. Svoboda, M. Sweany, M. Szydagis, D. Taylor, B. Tennyson, D. R. Tiedt, M. Tripathi, S. Uvarov, J. R. Verbus, N. Walsh, R. Webb, J. T. White, D. White, M. S. Witherell, M. Wlasenko, F. L. H. Wolfs, M. Woods, and C. Zhang, "First results from the lux dark matter experiment at the sanford underground research facility," *Phys. Rev. Lett.*, vol. 112, p. 091303, Mar 2014.

[15] E. Aprile, J. Aalbers, F. Agostini, M. Alfonsi, F. D. Amaro, M. Anthony, F. Arneodo, P. Barrow, L. Baudis, B. Bauermeister, M. L. Benabderrahmane, T. Berger, P. A. Breur, A. Brown, A. Brown, E. Brown, S. Bruenner, G. Bruno, R. Budnik, L. Bütikofer, J. Calvén, J. M. R. Cardoso, M. Cervantes, D. Cichon, D. Coderre, A. P. Colijn, J. Conrad, J. P. Cussonneau, M. P. Decowski, P. de Perio, P. Di Gangi, A. Di Giovanni, S. Diglio, G. Eurin, J. Fei, A. D. Ferella, A. Fieguth, W. Fulgione, A. Gallo Rosso, M. Galloway, F. Gao, M. Garbini, R. Gardner, C. Geis, L. W. Goetzke, L. Grandi, Z. Greene, C. Grignon, C. Hasterok, E. Hogenbirk, J. Howlett, R. Itay, B. Kaminsky, S. Kazama, G. Kessler, A. Kish, H. Landsman, R. F. Lang, D. Lellouch, L. Levinson, Q. Lin, S. Lindemann, M. Lindner, F. Lombardi, J. A. M. Lopes, A. Manfredini, I. Mariş, T. Marrodán Undagoitia, J. Masbou, F. V. Massoli, D. Masson, D. Mayani, M. Messina, K. Micheneau, A. Molinario, K. Morå, M. Murra, J. Naganoma,

K. Ni, U. Oberlack, P. Pakarha, B. Pelssers, R. Persiani, F. Piastra, J. Pienaar, V. Pizzella, M.-C. Piro, G. Plante, N. Priel, L. Rauch, S. Reichard, C. Reuter, B. Riedel, A. Rizzo, S. Rosendahl, N. Rupp, R. Saldanha, J. M. F. dos Santos, G. Sartorelli, M. Scheibelhut, S. Schindler, J. Schreiner, M. Schumann, L. Scotto Lavina, M. Selvi, P. Shagin, E. Shockley, M. Silva, H. Simgen, M. v. Sivers, A. Stein, S. Thapa, D. Thers, A. Tiseni, G. Trinchero, C. Tunnell, M. Vargas, N. Upole, H. Wang, Z. Wang, Y. Wei, C. Weinheimer, J. Wulf, J. Ye, Y. Zhang, and T. Zhu, "First dark matter search results from the xenon1t experiment," *Phys. Rev. Lett.*, vol. 119, p. 181301, Oct 2017.

[16] C. Amole, M. Ardid, D. M. Asner, D. Baxter, E. Behnke, P. Bhattacharjee, H. Borsodi, M. Bou-Cabo, S. J. Brice, D. Broemmelsiek, K. Clark, J. I. Collar, P. S. Cooper, M. Crisler, C. E. Dahl, S. Daley, M. Das, F. Debris, N. Dhungana, J. Farine, I. Felis, R. Filgas, M. Fines-Neuschild, F. Girard, G. Giroux, M. Hai, J. Hall, O. Harris, C. M. Jackson, M. Jin, C. B. Krauss, M. Lafrenière, M. Laurin, I. Lawson, I. Levine, W. H. Lippincott, E. Mann, J. P. Martin, D. Maurya, P. Mitra, R. Neilson, A. J. Noble, A. Plante, R. B. Podviianiuk, S. Priya, A. E. Robinson, M. Ruschman, O. Scallon, S. Seth, A. Sonnenschein, N. Starinski, I. Štekl, E. Vázquez-Jáuregui, J. Wells, U. Wichoski, V. Zacek, and J. Zhang, "Dark matter search results from the pico-2l c_3f_8 bubble chamber," *Phys. Rev. Lett.*, vol. 114, p. 231302, Jun 2015.

[17] C. Amole, M. Ardid, D. M. Asner, D. Baxter, E. Behnke, P. Bhattacharjee, H. Borsodi, M. Bou-Cabo, S. J. Brice, D. Broemmelsiek, K. Clark, J. I. Collar, P. S. Cooper, M. Crisler, C. E. Dahl, S. Daley, M. Das, F. Debris, N. Dhungana, S. Fallows, J. Farine, I. Felis, R. Filgas, F. Girard, G. Giroux, A. Grandison, M. Hai, J. Hall, O. Harris, M. Jin, C. B. Krauss, M. Lafrenière, M. Laurin, I. Lawson, I. Levine, W. H. Lippincott, E. Mann, D. Maurya, P. Mitra, R. Neilson, A. J. Noble, A. Plante, R. B. Podviianiuk, S. Priya, E. Ramberg, A. E. Robinson, R. Rucinski, M. Ruschman, O. Scallon, S. Seth, P. Simon, A. Sonnenschein, I. Štekl, E. Vázquez-Jáuregui, J. Wells, U. Wichoski, V. Zacek, J. Zhang, and I. A. Shkrob, "Dark matter search results from the pico-60 cf_3I bubble chamber," *Phys. Rev. D*, vol. 93, p. 052014,

Mar 2016.

[18] T. Lis, "Preparation, structure, and magnetic properties of a dodecanuclear mixed-valence manganese carboxylate," *Acta Crystallographica Section B Structural Crystallography and Crystal Chemistry*, vol. 36, pp. 2042–2046, Sep 1980.

[19] G. Chaboussant, A. Sieber, S. Ochsenbein, H.-U. Güdel, M. Murrie, A. Honecker, N. Fukushima, and B. Normand, "Exchange interactions and high-energy spin states in mn_{12}-acetate," *Phys. Rev. B*, vol. 70, p. 104422, Sep 2004.

[20] J. R. Friedman and M. P. Sarachik, "Single-Molecule Nanomagnets," *Annual Review of Condensed Matter Physics*, vol. 1, pp. 109–128, Aug 2010.

[21] K. Mertes, Y. Suzuki, M. Sarachik, Y. Myasoedov, H. Shtrikman, E. Zeldov, E. Rumberger, D. Hendrickson, and G. Christou, "Mn12-acetate: a prototypical single molecule magnet," *Solid State Communications*, vol. 127, pp. 131–139, Jul 2003.

[22] J. R. Friedman, M. P. Sarachik, J. Tejada, and R. Ziolo, "Macroscopic measurement of resonant magnetization tunneling in high-spin molecules," *Phys. Rev. Lett.*, vol. 76, pp. 3830–3833, May 1996.

[23] S. McHugh, R. Jaafar, M. P. Sarachik, Y. Myasoedov, A. Finkler, H. Shtrikman, E. Zeldov, R. Bagai, and G. Christou, "Effect of quantum tunneling on the ignition and propagation of magnetic avalanches in mn_{12} acetate," *Phys. Rev. B*, vol. 76, p. 172410, Nov 2007.

[24] P. C. Bunting, G. Gratta, T. Melia, and S. Rajendran, "Magnetic bubble chambers and sub-gev dark matter direct detection," *Phys. Rev. D*, vol. 95, p. 095001, May 2017.

[25] A. Hernández-Mínguez, J. M. Hernandez, F. Macià, A. García-Santiago, J. Tejada, and P. V. Santos, "Quantum magnetic deflagration in mn_{12} acetate," *Phys. Rev. Lett.*, vol. 95, p. 217205, Nov 2005.

[26] R. Sessoli, D. Gatteschi, A. Caneschi, and M. A. Novak, "Magnetic bistability in a metal-ion cluster," *Nature*, vol. 365, pp. 141–143, Sep 1993.

[27] A. D. Kent, Y. Zhong, L. Bokacheva, D. Ruiz, D. N. Hendrickson, and M. P. Sarachik, "Low temperature magnetic hysteresis in Mn12-acetate single crystals," *Journal of Applied Physics*, vol. 87, pp. 5493–5495, May 2000.